Strong Physical Contrasts across Two Mid-lithosphere Discontinuities beneath the Northwestern United States: Evidence for Cratonic Mantle Metasomatism

Tianze Liu[1], Emily J. Chin[2], Peter Shearer[1]

[1]Institute of Geophysics and Planetary Physics, Scripps Institution of Oceanography, UC San Diego, La Jolla, CA, USA
[2]Geosciences Research Division, Scripps Institution of Oceanography, UC San Diego, La Jolla, CA, USA

Key Points:

- Two mid-lithosphere discontinuities at ~ 89 and ~ 115 km depth exist beneath the eastern Wyoming craton and southwestern Superior craton.
- The shallow and deep interfaces represent isotropic velocity drops of 2–9% and 3–10%, respectively.
- The shallow and deep interfaces may represent the metasomatic front and the onset of carbonated partial melting, respectively.

Corresponding author: Tianze Liu, `tianzeliu@gmail.com`

Abstract

Mid-lithosphere discontinuities are seismic interfaces likely located within the lithospheric mantle of stable cratons, which typically represent velocities decreasing with depth. The origins of these interfaces are poorly understood due to the difficulties in both characterizing them seismically and reconciling the observations with thermal-chemical models of cratons. Metasomatism of the cratonic lithosphere has been reported by numerous geochemical and petrological studies worldwide, yet its seismic signature remains elusive. Here, we identify two distinct mid-lithosphere discontinuities at ~ 89 and ~ 115 km depth beneath the eastern Wyoming craton and the southwestern Superior craton by analyzing seismic data recorded by two longstanding stations. Our waveform modeling shows that the shallow and deep interfaces represent isotropic velocity drops of 2–9% and 3–10%, respectively, depending on the contributions from changes in radial anisotropy and density. By building a thermal-chemical model including the regional xenolith thermobarometry constraints and the experimental phase-equilibrium data of mantle metasomatism, we show that the shallow interface probably represents the metasomatic front, below which hydrous minerals such as amphibole and phlogopite are present, whereas the deep interface may be caused by the onset of carbonated partial melting. The hydrous minerals and melts are products of mantle metasomatism, with CO_2-H_2O-rich siliceous melt as a probable metasomatic reagent. Our results suggest that mantle metasomatism is probably an important cause of mid-lithosphere discontinuities worldwide, especially near craton boundaries, where the mantle lithosphere may be intensely metasomatized by fluids and melts released by subducting slabs.

Plain Language Summary

Based on xenolith and seismic-tomography evidence, the mantle lithospheres of stable cratons were commonly believed to be contiguous bodies with low temperatures and low content of volatile and incompatible elements, which are critical for the longevity of cratons. Nonetheless, in recent decades, many studies using scattered-wave imaging methods (e.g., receiver-function techniques) detected interfaces typically representing significant seismic-velocity reductions with depth within the mantle lithosphere of many cratons globally ("mid-lithosphere discontinuities" or MLDs). The sizes of the velocity reductions at the MLDs usually require the presence of significant volumes of hydrous minerals or even volatile-rich partial melts, which challenges the canonical compositional model of cratonic mantle lithospheres. The volatile-bearing phases causing MLDs likely originate from mantle metasomatism, a process widely documented yet poorly understood due to limited xenolith evidence. Here, we conduct a detailed case study of the MLDs beneath the northwestern United States and find that the two MLDs beneath the study area can be explained with a metasomatic front and the onset of carbonated partial melting, which are likely products of melt-assisted mantle metasomatism. Our results suggest mantle metasomatism as a likely origin of MLDs and the possibility of using seismic techniques to better characterize mantle metasomatism beneath cratons.

1 Introduction

Cratons are long-lived continental blocks having experienced little internal deformation since their formation in the Precambrian. The longevity of cratons has been attributed to their mantle lithosphere having: (1) a low viscosity due to low temperatures and low water content, which resists convective removal, and (2) neutral buoyancy due to chemical depletion, which inhibits subduction (Sleep, 2005). The low temperatures of cratonic mantle lithospheres have been imaged as high-velocity, low-attenuation bodies by numerous seismic tomography studies (e.g., Panning & Romanowicz, 2006; Dalton et al., 2008; Schaeffer & Lebedev, 2013), and the chemically depleted nature of cratonic mantle lithospheres is revealed by global mantle xenolith data (Lee et al., 2011).

These results have established high seismic velocities and high degrees of chemical depletion as two hallmarks of the lithospheric mantle beneath cratons.

However, a growing body of evidence across different disciplines is challenging the canonical view that cratonic mantle lithospheres are contiguous bodies with high seismic velocities and high degrees of chemical depletion: Seismological studies employing different types of scattered-wave methods consistently detect discontinuities within the mantle lithospheres beneath cratons, usually defined as the depth extent of the high-velocity anomaly in seismic tomography models, across different continents (e.g., Savage & Silver, 2008; Abt et al., 2010; Ford et al., 2010; Miller & Eaton, 2010; Sodoudi et al., 2013; Wirth & Long, 2014; S. M. Hansen et al., 2015; Ford et al., 2016; Tharimena et al., 2017; Krueger et al., 2021; Liu & Shearer, 2021), although a recent study doubted the existence of such interfaces beneath the contiguous U.S. (Kind et al., 2020). These intra-lithosphere interfaces are commonly termed mid-lithosphere discontinuities (MLDs) and are found to predominantly represent velocity reductions with depths up to 12% (Wölbern et al., 2012), which suggests that cratonic mantle lithospheres contain fine-scale structures beyond the resolution of typical tomography images. On the other hand, metasomatism of cratonic mantle lithospheres caused by hydrous fluids or siliceous melts has been documented globally based primarily on mantle xenolith data (e.g., Pearson et al., 1995; Downes et al., 2004; Carlson et al., 2004; Bell et al., 2005; Ionov et al., 2006; Simon et al., 2007), suggesting that mantle metasomatism is likely pervasive beneath cratons and thus has a profound effect on the internal structures of their mantle lithospheres.

Mantle metasomatism can reduce the seismic velocities of cratonic mantle lithosphere by precipitating low-velocity hydrous and carbonate minerals (e.g., amphiboles, phlogopite, and magnesite) and thus has been proposed as a possible cause of MLDs by some seismological studies (e.g., Wölbern et al., 2012; Krueger et al., 2021). Specifically, the global survey of Krueger et al. (2021) showed a correlation between MLD detection and thermotetonic ages of cratons, providing evidence for a metasomatism origin of MLDs. A recent series of experimental investigations further established the stability pressure-temperature fields of amphiboles, phlogopite, magnesite, and carbonated melt in cratonic mantle lithospheres fluxed by various metasomatic reagents (e.g., CO_2-H_2O-rich melts and CO_2-rich aqueous fluids; Saha et al., 2018; Saha & Dasgupta, 2019; Saha et al., 2021). Nonetheless, seismic observations have shown that MLDs are spatially highly variable in both depth and amplitude beneath the contiguous U.S. (Liu & Shearer, 2021) and around the globe (Krueger et al., 2021), suggesting that MLDs in different regions likely have distinct origins closely associated with regional tectonic evolution. Therefore, the connection between the origins of MLDs and mantle metasomatism can only be confidently established through case-by-case studies incorporating local geophysical and petrological observations and mineral-physical constraints, an outstanding research gap waiting to be filled.

In addition to causing MLDs, mantle metasomatism likely plays a key role in the evolution of cratons. The introduction of fluids and metasomatic minerals can significantly weaken cratonic mantle lithospheres and thus facilitate their removal by mantle convection, plumes, and slab subduction, which could lead to the destruction of cratons (Lee et al., 2011). The metasomatic density reduction in a certain depth range of the cratonic mantle lithosphere could cause density inversions (high-density materials over low-density materials), which could also destabilize cratonic lithospheres and thus promote their convective removal, similar to the effects of ecologitized lower crusts (Hacker et al., 2015). Understanding the global prevalence of these processes requires constraints on the spatial extent of mantle metasomatism, which are traditionally difficult to acquire due to the scarcity and uneven distribution of mantle-xenolith samples. Therefore, using seismically observed MLDs as proxies for mantle metasomatism can improve understanding of the role played by mantle metasomatism in the life cycles of continents. Achieving this goal also requires a better understanding of the connection between MLDs and mantle metasomatism.

Here, we conduct a detailed case study of the northwestern U.S. cratons to establish the connection between MLDs and mantle metasomatism. We first image two distinct MLDs beneath two longstanding stations located in the eastern Wyoming craton and southwestern Superior craton using teleseismic SH reverberations. We then associate the two MLDs with different metasomatic phases using a regional thermal-chemical model that incorporates xenolith thermobarometry constraints and experimental phase-equilibrium data and discuss the implications of our findings on the study of MLDs and craton evolution.

2 Seismic characterizations of the MLDs

2.1 Data and methods

We use seismic waveform data recorded by two longstanding stations RSSD and ECSD located in the eastern Wyoming craton and southwestern Superior craton, respectively (near the western and eastern borders of the state of South Dakota; Figs. 1b and c). We choose the two stations for four reasons: (1) They are permanent stations with high data quality and long recording times (>15 years), providing large numbers of earthquake records to form stable waveform stacks. (2) They are located on two different Archean cratons (Figs. 1b and c) and thus enable us to resolve potential lateral variations in lithospheric structure within the North American craton. (3) Eilon et al. (2018) presented one-dimensional (1D) velocity profiles down to 300 km depth for the two stations (hereafter "EFD18") estimated using a joint inversion of P-receiver functions (PRFs), S-receiver functions (SRFs), and Rayleigh-wave dispersion data. These models provide us with reference velocity models to map the waveform stacks from the time domain to the depth domain and also offer the opportunity to directly compare our MLD images with those from previous studies. (4) The waveform stacks of the two stations from two narrow back-azimuth windows nearly 90° apart (southwest and northwest) show consistent features in the time windows corresponding to the lithosphere mantle (Figs. 1c and d), suggesting little contribution from azimuthal anisotropy and lateral heterogeneity. These observations allow us to model the observed waveforms using 1D velocity models with vertical transverse isotropy (VTI), the simplest form of seismic anisotropy (see Section 2.3.4 for details).

We use the teleseismic SH-reverberation method to image the structures above 175 km depth beneath RSSD and ECSD (Shearer & Buehler, 2019; Liu & Shearer, 2021). Specifically, we use only events deeper than 175 km to eliminate the ambiguity between source-side and receiver-side scattering (Fig. 2a) following Liu and Shearer (2021). We filter the SH-component waveforms to below 0.1 Hz, align the traces to their S arrival times, and remove traces with low signal-noise ratios, prolonged source wavelets, and abnormally strong coda energy (see Liu and Shearer (2021) for details about the data-processing workflow). Because *ScS* arrives in the same time window as the reverberation phases for lithospheric discontinuities in the epicentral distance range 65–85° (Figure 4a in Liu and Shearer (2021)), we further remove the events in this distance range to minimize the interference of *ScS*. At the expense of reducing the number of available events, this procedure is likely more effective in reducing *ScS* contamination and avoids possible processing artifacts compared to muting *ScS* energy using predicted travel times as applied in Liu and Shearer (2021). We then map the traces from the time domain to the depth domain using EFD18 and stack them linearly to form the depth-domain stacks in Fig. 1a. We hereafter term arrivals representing impedance increasing with depth "positive" and color them blue, and arrivals representing impedance decreasing with depth "negative" and color them red (Fig. 1a). Because we directly stack the traces without applying source normalization as in receiver-function techniques, the reference pulses of our stacks have sidelobes that vary with the traces included in the stacks (Figs. 1a and 2c and d). Nonetheless, the reference pulses can be estimated from the observed waveforms and used to generate synthetic waveforms for waveform modeling (Section 2.3.3).

2.2 Observations

2.2.1 Overview

The depth-domain stacks of both stations show a positive peak at ~ 50 km depth, although the peak of RSSD is very weak and barely distinguishable from the trailing sidelobe of the reference pulse (Fig. 1a). The depths of these peaks agree very well with the Moho depths in EFD18 (gray curves in Fig. 1a) and thus likely represent the Moho beneath the two stations.

Below the Moho at RSSD, we observe a strong and broad negative arrival at 50–100 km consisting off two peaks at $\sim$60 km and $\sim$85 km depth (Fig. 11a). Considering the width of the trailing sidelobe of the reference pulse, the shallow negative peak may largely consist of the Moho sidelobe, but the deep negative peak is unlikely to be affected by the sidelobe and thus likely represents a negative interface at $\sim$85 km depth (Fig. 1a). Below this interface, we observe another distinct yet weak negative arrival at $\sim$115 km depth, which likely represents a deeper negative interface (Fig. 1a). At greater depths, we observe a positive arrival followed by a negative arrival. We refrain from interpreting these arrivals because event hypocenter errors and the finite widths of *ScS* and *sS* arrivals may cause their energy to leak into the bottom part of the image. At ECSD, we observe a negative peak at $\sim$85 km, which is too far away from the Moho to be its sidelobe and thus likely represents a negative interface (Fig. 1a). Immediately below this interface, we observe a positive peak, which could partly be due to the sidelobe of the negative phase above it. At greater depths, we observe a strong negative arrival at $\sim$120 km and a weaker one at $\sim$150 km (Fig. 1a). Following the argument for RSSD, we interpret the former as a negative interface at $\sim$120 km while leaving the interpretation of the latter open. We will hereafter refer to the two negative interfaces with definitive interpretations beneath the two stations as "MLD1" and "MLD2", respectively, because they likely reside within the lithosphere as defined by the high-velocity region extending to $\sim$200 km depth beneath the North America cratons (e.g., Schaeffer and Lebedev (2013)).

2.2.2 Comparison with previous studies

Although our Moho depths at both stations agree well with those from EFD18, our mantle structures appear to be significantly different. At RSSD, our results show at least two distinct negative interfaces at $\sim$85 km and $\sim$115 km depth, whereas EFD18 shows a broad negative velocity gradient zone between the Moho and $\sim$100 km depth, with the strongest gradient immediately below the Moho (Fig. 1a). This broad negative velocity gradient zone is underlain by a equally broad velocity recovery zone extending to $\sim$150 km depth. Intriguingly, the depths of the two MLDs beneath RSSD appear to agree with the two MLDs identified on the SRF stacks of two different back-azimuth groups at the same station (Figure 6b in Krueger et al. (2021)). The discrepancy between EFD18 and Krueger et al. (2021) is difficult to understand because the constraints on mantle discontinuities in both studies come from SRFs. Whereas in Krueger et al. (2021), the SRFs of each back-azimuth group only show one of the two MLDs beneath RSSD, our results appear to be largely consistent between the two best-sampled back-azimuth windows (Fig. 2c). We speculate that this discrepancy may be due to the smaller reflection-point-station distances for SH reverberations compared to the conversion-point-station distances for SRFs, which could cause the SRFs from different back azimuths to sample different structures. This reason was also used by Krueger et al. (2021) to explain the discrepancy between their results for the two back-azimuth groups. In summary, at RSSD the general agreement on the depths of MLD1 and MLD2 between our results and those from Krueger et al. (2021) indicates that the two interfaces are real features instead of imaging artifacts.

At ECSD, we find two MLDs at ∼85 km and ∼120 km depth, whereas EFD18 showed two low-velocity layers bounded by broad velocity gradients with the maximum negative velocity immediately below the Moho and at ∼120 km depth, respectively (Fig. 1a). Our MLD2 thus may correspond to the deeper negative velocity gradient zone in EFD18, whereas our MLD1 does not seem to agree with EFD18 in the same depth range (Fig. 1a). Krueger et al. (2021) did not identify any robust MLDs beneath ECSD, though their stack in Figure 6c appears to show a weak and broad negative peak at 125–145 km depth, which was not identified probably because the amplitude of the peak is below their prescribed uncertainty range. This peak may correspond to our MLD2 due to their similar depths.

We also compare our results with the PRF images at the two stations from Ford et al. (2016). The Moho depths estimated by Ford et al. (2016) at RSSD and ECSD are ∼53 km and ∼50 km respectively, consistent with our results (Fig. 1a). Below the Moho, Ford et al. (2016) found two interfaces with significant negative azimuth-invariant components at ∼86 km and ∼139 km depths beneath RSSD and one such interface at ∼135 km depth beneath ECSD. The two interfaces beneath RSSD may correspond to our MLD1 and MLD2, and the interface beneath ECSD may correspond to our MLD2, though the depths of the deeper MLDs from Ford et al. (2016) are less consistent with the depths of our MLD2s possibly due to complexities in the velocity models used for converting time to depth. Ford et al. (2016) also resolved multiple interfaces below the Moho with significant azimuthal variation beneath the two stations, which appear to disagree with the azimuth-invariant feature of our waveform stacks (Figs. 2b–d).

Using the *SS*-precursor technique, Tharimena et al. (2017) imaged the LAB beneath the North America continental interior at a depth of 170–180 km and found no MLDs beneath North America, which appear to contradict our results (Figure 2 in Tharimena et al. (2017)). This discrepancy likely results from the use of waveform stacks from all *SS* records that bounced within the study area, which represents the 1D average lithosphere structure of the whole continent. The Tharimena et al. (2017) waveform stack thus may have failed to capture the MLDs beneath North America, which were shown to be spatially heterogeneous structures at least beneath the contiguous US (Liu & Shearer, 2021).

2.2.3 Evaluation of azimuthal variation

Since we use only events deeper than 175 km, the back azimuths of the events are limited to three narrow back-azimuth corridors containing three major subduction zones with deep slab penetration: South America, southwest Pacific, and northwest Pacific (Figs. 2b–d). Fortunately, the three back-azimuth windows are approximately 90° apart (Figs. 2b–d), allowing us to evaluate the degree of azimuthal variation of our observed MLD signals despite the poor back-azimuth coverage of our events. We choose to compare the waveform stacks of the southwest-Pacific (240–270°) and northwest-Pacific (300–330°) events because the two corridors contain the most events (Figs. 2b–d).

At RSSD, the sidelobes of the reference pulses are significantly different between the waveform stacks of the two event groups likely due to the different events included in the stacks (Fig. 2c). The signals at 20–35 s, which include the Moho arrival and its sidelobe, also appear inconsistent between the two groups. This discrepancy may be due to lateral heterogeneity in Moho structures beneath the station (Fig. 2c). Nonetheless, the waveforms at 35–60 s, which contain the arrivals of MLD1 and MLD2, are generally consistent between the two groups, although the northwest-Pacific stack shows more high-frequency variation and greater uncertainties likely due to its significantly lower stacking fold compared to the southwest-Pacific stack (Fig. 2c). This contrast in azimuthal consistency between the Moho and MLD arrivals provides further evidence that the MLD signals are unlikely caused by Moho sidelobes. At 60–75 s, the discrepancy between the two stacks increases again, which could be due to anisotropy, lateral heterogneity, or leakage of *ScS* and *sS* energy. We will not further discuss these features in this paper.

At ECSD, despite the differences in reference-pulse sidelobes, the stacks of the two back-azimuth groups show consistent Moho, MLD1, and MLD2 arrivals (Fig. 2d), indicating a weaker degree of lateral heterogeneity compared to RSSD. In addition, the negative arrival at ∼65 s, which corresponds to the arrival at ∼150 km depth in the depth-domain stack, also appears to be consistent between the two back-azimuth groups, suggesting that it may also represent a negative interface without azimuthal variation (Figs. 2a and 2d). Nonetheless, we choose not to interpret this feature due to possible contamination from *ScS* and *sS*. In summary, our azimuthal analysis indicates that MLD1 and MLD2 beneath the two stations can be modeled as azimuth-invariant negative interfaces. Therefore, we will hereafter only use the observed waveform stack computed using all events to compare with synthetic waveforms. We also caution that our results cannot eliminate the possibility of the presence of azimuthal anisotropy in the mantle beneath the two stations because (1) our events only have limited back-azimuth coverage (Figs. 2c and d), and (2) some azimuthally anisotropic models may not show as strong manifestations for SH-reverberation observations as for other observations (e.g., PRF; Ford et al., 2010)

2.3 Waveform modeling

2.3.1 Source wavelets and initial models

To further constrain the size of velocity drops required to explain the MLDs beneath RSSD and ECSD, we compute synthetic waveforms using 1D isotropic and anisotropic velocity models and compare them with the observed waveforms. The synthetic waveforms are computed in two steps. First, we compute Green's functions using the reflectivity method (Kennett, 2009). Second, we estimate the source wavelet from the observed waveform and convolve it with the Green's function to produce the synthetic waveform. To estimate the source wavelet, we assume that the observed signal before a certain time (t_0) consists solely of the source wavelet and that the source wavelet after t_0 tapers to zero exponentially with a characteristic time t_c (gray dotted curves in Figs. 3b and 4b). Because the Moho phase arrives close to the reference pulse (Figs. 2c and d), the choices of t_0 and t_c significantly affect the Moho phase on the synthetic waveforms. We thus estimate t_0 and t_c by fitting the synthetic Moho phases to the observed ones.

We first tried using EFD18 to compute the synthetic waveforms and found that the synthetics significantly overpredict the amplitudes of the Moho phase for both stations regardless of the t_0 and t_c choices, although the arrival times are relatively well captured (light gray solid curves in Figs. 3b and 4b). We thus reduce the amplitude of the Moho phase while keeping its arrival time unchanged by replacing the sharp Moho in EFD18 with a linear velocity gradient zone spanning a depth range containing the Moho. We manually adjust the depth range of the Moho gradient zone, t_0, and t_c until a reasonable fit to the observed Moho phase is achieved. We then replace the mantle part of the model with a homogeneous half space having a velocity equal to the velocity immediately below the Moho (dark gray curves in Figs. 3a and 4a). We will use this model with a homogeneous mantle velocity as the initial model for building models with negative velocity gradient zones (NVGs) in the mantle. The companion source wavelet (dotted gray curves in Figs. 3b and 4b) will be used for computing the synthetic waveforms for all models. Our initial models produce significantly weaker Moho phases than the EFD18 models for both stations, which are more consistent with our observed Moho phases (dark gray, light gray, and black curves in Figs. 3b and 4b).

The more gradual Moho suggested by our SH-reverberation observations compared with EFD18 may be due to two reasons. First, the Moho in EFD18 is constrained using PRFs, whose Moho P-to-S conversion points are closer to the stations than the Moho reflection points of our SH-reverberation observations, causing PRFs to be less sensitive to lateral variations in Moho depth and sharpness, which likely has a smoothing effect on our Moho phases. This interpretation is supported by the apparent lateral variation in Moho structure shown by the stacks of events from two back-azimuth groups at RSSD (Fig. 2c). Second, PRF conversion amplitudes are mostly sensitive to velocity contrasts across interfaces, whereas SH-reverberation amplitudes are sensitive to both contrasts in V_s and density. Therefore, a reduced density contrast across the Moho could weaken the SH Moho reflection without significantly affecting the P-to-S conversion. Such a reduced density contrast could be caused by ecologitization of the lower crust (Hacker et al., 2015).

2.3.2 Trade-offs between model parameters

In a stratified VTI medium, changes in anisotropy alone (no isotropic V_s drop) could cause negative SH reflections. Hereafter, we will define a medium with the velocity of *horizontally traveling and horizontally polarized S waves* (V_{SH}) greater than that of *horizontally traveling and vertically polarized S waves* (V_{SV}) as a medium with positive radial anisotropy. This parametrization of anisotropy is also commonly used in surface-wave studies (e.g., Panning & Romanowicz, 2006). An increase in radial anisotropy is thus defined as an increase in $V_{SH}-V_{SV}$. Here, we choose to characterize the amount of radial anisotropy using anisotropy amplitude a defined as the difference between V_{SH} and V_{SV} normalized by their mean (hereafter "average V_s" $\bar{V}_s$):

$$\begin{aligned} a &= \frac{V_{SH} - V_{SV}}{\bar{V}_s} \\ &= \frac{2(V_{SH} - V_{SV})}{(V_{SH} + V_{SV})} \end{aligned}$$

This definition was used by some studies analyzing anisotropic signatures of P-receiver functions (e.g., Schulte-Pelkum & Mahan, 2014). Another way of characterizing radial anisotropy is using the "radially anisotropic parameter" ξ defined as:

$$\xi = \frac{V_{SH}^2}{V_{SV}^2}$$

This definition is commonly used in surface-wave tomography studies (e.g., Panning & Romanowicz, 2006). It can be shown that:

$$\xi \approx 1 + 2a$$

In Section 2.3.4, we will convert our estimated anisotropy amplitude as functions of depth to ξ to facilitate the comparison with previous tomography results. In VTI mediums, in addition to a or ξ, another parameter is needed to characterize the shape of the phase velocity surfaces. Here, we choose to use Kawakatsu's fifth parameter η_κ, which measures the deviation of the phase-velocity surfaces from an ellipse (Kawakatsu, 2016a). We will assume $\eta_\kappa = 1$, which indicates perfectly elliptical phase-velocity surfaces, for all our anisotropic models.

Our synthetic tests show that an increase in radial anisotropy with depth can also generate negative SH reflections similar to a decrease in isotropic V_s with depth (Fig. 5a). Specifically, in the case of a zero gradient-zone thickness, a 7.5% increase in radial anisotropy generates almost the same reflection phase as a 5.0% decrease in isotropic V_s (solid red and purple curves in Fig. 5a). This behavior can be conceptually understood using the phase-velocity and polarization surfaces (Fig. 5b). In a VTI medium, the SH waves remain decoupled from the P and SV waves as in the case of isotropy, and the velocity of SH waves is reduced for near-vertically traveling waves (pumpkin-shaped velocity surface; Fig. 5b). Because in SH reverberations, the incident angles of the downgoing waves are usually small ($\sim 20°$ at the Moho), an increase in radial anisotropy with depth is equivalent to a decrease in isotropic V_s with depth and thus can also generate negative SH reflections. Therefore, a trade-off exists between the changes in isotropic V_s and radial anisotropy estimated from observed SH-reverberation waveforms, which needs to be considered in the waveform modeling (Section 2.3.4).

In addition, density reductions across the MLDs may also contribute to the observed signals because SH-reflection amplitudes are controlled by contrasts in impedance, the product of V_s and density. Similar to the case with an increase in anisotropic amplitude, we compute synthetic waveforms using models with a 5% isotropic V_s drop or density drop over 0, 8 and 15 km depth and compare them (Fig. 5c). The results show that the SH-reflection amplitude generated by the density drop is slightly higher than the one generated by the V_s drop given the same gradient-zone thickness, and that the amplitude decreases with increasing gradient-zone thickness for both density and V_s drops (Fig. 5c). We note that the degree of density drop assumed here may be unrealistic because a lithosphere with a high-density layer overlying a low-density one (density inversion) is gravitationally unstable and could lead to the convective removal of the dense layer (Jull & Kelemen, 2001). We will further discuss the trade-offs between V_s and density reductions across MLDs in Section 2.3.5 and the dynamic viability of models with density inversions in Section 4.4.

2.3.3 Isotropic models

We first consider the simplest case where the observed MLD arrivals are caused only by isotropic V_s drops. To obtain the best-fitting models, we insert MLDs with various properties into our reference models, compute the synthetic waveforms, and compare them with the observations. Specifically, we assume that the mantle part of the model contains two MLDs represented by linear negative velocity gradients (NVGs) and a linear positive velocity gradient (PVG) between the two MLDs, with each velocity gradient parameterized by three parameters: depth, percentage velocity increase/decrease, and thickness. We then use a three-step grid-search method to find the best-fitting model. First, we assume that the model contains only MLD1 and search for its parameters that minimize the root-mean-square misfit (hereafter "misfit" for simplicity) in a 10 s window centered at the arrival time of the MLD1 arrival (40 s for both stations; yellow dashed lines in Figs. 3b and 4b). The resulting best-fit models, waveforms, and parameter combinations are shown in yellow in Figs. 3 and 4. Second, we assume that the model contains only MLD2 and search for parameters minimizing the misfit in a 10 s window centered at the arrival time of the MLD2 arrival (52.5 s and 55 s for RSSD and ECSD, respectively; orange dashed lines in Figs. 3b and 4b). The results are shown in orange in Figs. 3 and 4. Third, we assume that the model contains both MLD1 and MLD2 with a PVG between them and fix the depth of MLD1 and thicknesses of MLD1 and MLD2 at the best-fit values found in the previous steps while searching for the parameters of the PVG that minimize the misfit in the time window enclosing both the windows for MLD1 and MLD2 defined in the previous steps (35–57.5 s and 35–60 s for RSSD and ECSD, respectively). Due to the finite widths of our reference pulses (Figs. 3b and 4b), the amplitude of an MLD arrival may be affected by the addition of another one close in time. We thus search for the best-fit velocity drops at MLD1 and MLD2 again in a reduced range ($\pm 5\%$) around their previous best-fit values to obtain the final velocity-drop estimates for the two MLDs. The results of this final step are shown in red in Figs. 3 and 4.

To explore the well-known trade-off between the velocity contrast across a gradient zone and its thickness in modeling scattered-phase amplitudes (e.g., Mancinelli et al., 2017), we plot the misfit as a function of V_s drop and gradient-zone thickness at Step

One (MLD1) and Two (MLD2) for both stations, which shows strong trade-offs between the two parameters in all cases, with an increasing thickness requiring a greater velocity drop (Figs. 3c and 4c). We thus present two sets of parameter estimates for the two MLDs, one with no constraint on the gradient-zone thickness and the other with a zero gradient-zone thickness (first-order discontinuity). The results estimated without constraints on gradient-zone thickness are shown as transparent models, waveforms, and markers in Figs. 3 and 4, whereas models with a zero gradient-zone thickness are shown as opaque symbols. Given the positive trade-off between the gradient-zone thickness and V_s drop, the V_s-drop estimate in the case of a first-order discontinuity can be regarded as the lower bound of the size of V_s drop required to explain our observations (Figs. 3c and 4c). We further define the uncertainty of our V_s-drop estimates as the range where the misfits are within 0.01 from the best estimate in the case of a first-order discontinuity (error bars in Figs. 3c and 4). We choose 0.01 as the misfit threshold because it is the approximate uncertainty level of our waveform stacks (thick and thin black waveforms in Figs. 3b and 4b). We acknowledge that we likely underestimate the true V_s-drop uncertainties with our uncertainty definition because it does not account for the trade-off between the gradient-zone thickness and V_s drop; we instead characterize the latter with our two sets of estimates with and without constraints on the gradient-zone thickness.

For RSSD, when the MLD thicknesses are allowed to vary, Step One gives an MLD1 centered at 86 km with a V_s drop of 15% and a thickness of 22 km (transparent yellow models in Fig. 3a and cross in the top panel of Fig. 3c, which overlaps with the transparent red cross), and Step Two gives an MLD2 centered at 116 km with a V_s drop of 8% and a thickness of 0 km (transparent orange models in Fig. 3a and cross in Fig. 3c). In Step Three, the PVG is estimated to have no velocity increase and a thickness of 14 km, yielding a final depth of 110 km for MLD2 (transparent red model in Fig. 3a). Step Three also increases the V_s drop at MLD2 to 11% (transparent red cross in the bottom panel of Fig. 3c) likely because the trailing sidelobe of the MLD1 arrival (transparent yellow waveform in Fig. 3b) requires a greater amount of V_s drop at MLD2 to explain its amplitude. In contrast, when the MLD thicknesses are fixed at 0 km, Step One gives the same depth but a significantly smaller V_s drop of 8% for MLD1 (opaque yellow model in Fig. 3a and arrow in Fig. 3c), and Step Three slightly reduces it to 7% (opaque red arrow in the top panel of Fig. 3c). Step Three further yields a zero velocity increase for the PVG and a final depth of 116 km for MLD2 (opaque red model in Fig. 3a). For MLD1, the thick gradient zone with a greater V_s drop produces a slightly smaller misfit compared to the sharp gradient zone with a smaller V_s drop (Fig. 3c) likely because the former generates a broader arrival on the synthetic waveform, which is more consistent with the observation than the latter, although the difference between the two synthetic waveforms is largely within the uncertainty range of the observations (opaque and transparent red waveforms in Fig. 3b). This preference for a thicker gradient zone likely also causes the high uncertainty ($\pm 5\%$) for the V_s drop at MLD1 (Fig. 3c). In contrast, the best-fit gradient-zone thickness for MLD2 is zero even without explicit constraints likely due to the impulsive shape of the arrival (Fig. 3b), which probably also causes the small V_s drop uncertainty ($\pm 2\%$). In summary, at RSSD, MLD1 is possibly a thick gradient zone with a V_s drop greater than 7%, whereas MLD2 is likely a sharp discontinuity with a V_s drop of $\sim 8\%$.

For ECSD, when the MLD thicknesses are not fixed a priori, MLD1 is estimated to be at 88 km with a V_s drop of 5% and zero thickness, and MLD2 is constrained to be centered at 123 km with a V_s drop of 13% occurring over 17 km (Figs. 4a and c). The PVG between the two MLDs is again estimated to have no V_s increase. When the MLD thicknesses are fixed at zero, the V_s drop at MLD1 is slightly reduced to 4%, whereas the V_s drop at MLD2 is significantly reduced to 9% with its depth unchanged (Figs. 4a and c). For MLD1, the misfits given by the parameter combinations in our searching range are generally greater than the other cases likely because a positive peak at $\sim$35 s preceding the MLD1 arrival is not well fitted (Fig. 4b). We speculate that this positive peak may be due to a positive velocity gradient between the Moho and MLD1 not included in our models. For simplicity, we will not attempt to fit this feature in this paper. The high misfit likely also causes the relatively large V_s-drop misfit ($\pm 4\%$) for MLD1 (Fig. 4c). For MLD2, the thick gradient zone with a greater V_s drop yields a slightly smaller misfit than the sharp discontinuity with a smaller V_s drop (Fig. 4c), although the difference between the two synthetic waveforms is hardly visible (opaque and transparent red waveforms in Fig. 4b). The uncertainty of the V_s drop at MLD2 is estimated to be $\pm 3\%$ (orange error bar in Fig. 4c). In summary, at ECSD, MLD1 is likely a sharp interface with a V_s drop of $\sim 4\%$, whereas MLD2 may also be relatively sharp with a minimum V_s drop of $\sim 9\%$.

2.3.4 Anisotropic models

As mentioned in Section 2.3.2, both a reduction in isotropic V_s and an increase in radial anisotropy amplitude a can cause negative arrivals (Fig. 5). We thus quantify the trade-off between the two factors by fitting the observed waveforms using various 1D VTI models (Fig. 6). The synthetic waveforms are computed using the open-source software *Aniplane.jl*, which derives the displacement-stress matrix for each layer following Crampin (1981) and generates the synthetic waveforms using the reflectivity method (Kennett, 2009). We parameterize the models in the same way as in the isotropic case except that the thicknesses of both MLDs are fixed at zero, which gives the minimum isotropic V_s drops and increases in a required to produce the MLD arrivals. We assume that the model above MLD1 is isotropic and that the relative isotropic V_s reduction and the increase in a across the MLDs are linearly related by a factor c. For example, when $c = 2.0$, an MLD with a 5% isotropic V_s drop will have a 10% increase in a. Similarly, an interface with a 5% isotropic V_s increase will have a 10% decrease in a. This model is based on the assumption that physical mechanisms causing isotropic V_s drops (e.g., volatile-bearing phases) also cause increases in radial anisotropy. We then search for the best-fit model parameters (V_s drop and depth of MLD1, V_s increase and thickness of the PVG, and V_s drop of MLD2) around the best-fit parameters estimated for the isotropic case. Specifically, we consider two cases with $c = 1.0$ and 2.0 to explore the trade-off between the isotropic and anisotropic contributions to the MLD signals (Fig. 6).

The results show that the best-fit anisotropic models produce waveforms closely resembling those generated by the best-fit isotropic models while requiring significantly smaller isotropic V_s reductions (light and dark purple in Fig. 6). For RSSD, $c = 1.0$ yields isotropic V_s reductions of 5% for both MLD1 and MLD2 (light purple models in the left panel of Fig. 6a), whereas $c = 2.0$ gives V_s reductions of 4% for both interfaces (dark purple models in Fig. 6a). In the case of $c = 1.0$, ξ increases from 1.00 (isotropic) to ~ 1.10 at MLD1 and ~ 1.20 at MLD2 (light purple models in the middle panel of Fig. 6a), whereas when $c = 2.0$, ξ increases to ~ 1.20 at MLD1 and ~ 1.40 at MLD2 (dark purple models in the middle panel of Fig. 6a). For ECSD, $c = 1.0$ yields a model with isotropic V_s decreasing by 3% and 6% and ξ increasing to ~ 1.05 and ~ 1.20 at MLD1 and MLD2, respectively (light purple models in the middle panel of Fig. 6b). In the case of $c = 2.0$, the best-fit model has V_s reductions of 2% and 4% at MLD1 and MLD2, with ξ increasing to ~ 1.10 and ~ 1.30 respectively at the two interfaces (dark purple models in the middle panel of Fig. 6b). An interesting observation is that all best-fit anisotropic models show similar V_{SV} values (dashed models with lower values in the middle panels of Fig. 6) to those of the best-fit isotropic models (red models in the middle panels of Fig. 6) regardless of their anisotropy amplitudes. A likely explanation for this phenomenon is that in our VTI models, near-vertically traveling SH waves sample the portion of the SH phase-velocity surface close to its minimum (the zenith), where the velocities of SH and SV waves are equal (the SH and SV phase-velocity surfaces are tangent to each other at the zenith; Fig. 5b). This property of VTI mediums, combined with the fact that the SV velocity is constant across all directions (Fig. 5b), causes V_{SV}, the velocity of horizontally traveling SV waves in each layer, to be close to the corresponding phase velocities of the near-vertically traveling SH waves, which controls the SH reflection coefficients at the layer boundaries.

Since ξ is a parameter that has been reported by many surface-wave tomography studies that account for radial anisotropy, we compare our ξ profiles with the profiles extracted for the two stations from four well-known recent tomographic models: *SEMum-NA14* (hereafter *SEMum* for simplicity; dashed black model in the middle panels of Fig. 6; Yuan et al., 2014), *CSEM_North_America* (hereafter *CSEM* for simplicity; dotted black model in the middle panels of Fig. 6; Krischer et al., 2018), *GLAD-M25* (hereafter *GLAD* for simplicity; dashed gray model in the middle panels of Fig. 6; Lei et al., 2020), and *SAVANI_US* (hereafter *SAVANI* for simplicity; dotted gray model in the middle panels of Fig. 6; Porritt et al., 2021). The comparison shows that except for the depth ranges above MLD1 in the case with $c = 1.0$, our ξ is significantly greater than those given by all four models, which largely show $\xi < 1.10$ (middle panels of Fig. 6). Three possible factors may have contributed to this discrepancy: First, we may have overestimated the increases in anisotropy amplitude and thus ξ across the MLDs, which would imply greater isotropic V_s reductions at the MLDs than in the cases with $c = 1.0$ and 2.0 (Fig. 6). Second, our method may not have yielded the correct absolute anisotropy amplitude because SH reflection amplitudes are only sensitive to anisotropy contrasts across interfaces, whereas the surface-wave models may have underestimated the degree of anisotropy variation with depth due to the broad depth-sensitive kernels of surface-wave dispersion measurements. In this case, our ξ profiles should have similar mean values and variation trends as the surface-wave ξ profiles. Among the four surface-wave models, *SEMum* and *GLAD* show ξ increasing with depth in 50–150 km depth, whereas *CSEM* and *SAVANI* show ξ decreasing with depth middle panels of Fig. 6). Our results can thus become compatible with *SEMum* and *GLAD* if we reduce the mean values of our ξ profiles to the mean values of the surface-wave ξ profiles, which should have little effect on the synthetic waveforms. Third, other model assumptions may have caused the surface-wave models to underestimate the absolute ξ or its variation with depth in the mantle lithosphere. For example, Figure 1 of Kawakatsu (2016b) demonstrated that the phase velocity of fundamental-model Rayleigh waves at 30 s is not only sensitive to V_{SV} in the upper mantle but also η_κ in the crust and upper mantle as well as the velocity of horizontally-propagating P waves in the crust. Different previous surface-wave studies likely made different assumptions about these parameters, which could have contributed to the diversity of their resulting ξ profiles (middle panels of Fig. 6).

2.3.5 Models with density reductions

We explore the trade-off between isotropic V_s and density drops at the MLDs in a similar way as we did for changes in radial anisotropy. Specifically, we assume that density drops are linearly related to V_s drops by a factor c and search for the best-fit models assuming $c = 0.5$ and 1.0, which is based on the assumption that physical mechanisms causing V_s drops (e.g., volatile-bearing phases) also cause density drops (Fig. 7). The results show that when $c = 0.5$, the best-fit V_s drops across MLD1 and MLD2 beneath RSSD are reduced to 5% and 6% (2.5% and 3% density drops), respectively (left and middle panels of Fig. 7a). For ECSD, the V_s drops across MLD1 and MLD2 are 3% and 5% (1.5% and 5% density drops), respectively (left and middle panels of Fig. 7a). In the case of $c = 1.0$, the V_s reductions across MLD1 and MLD2 are both 4% (4% density drops) for RSSD (left and middle panels of Fig. 7a) and 2% and 4%(2% and 4% density drops), respectively, for ECSD (left and middle panels of Fig. 7b). Similar to the previous cases with changes in radial anisotropy, the best-fit waveforms generated using the models with density changes are almost identical to the corresponding best-fit waveforms with only isotropic V_s changes (right panels of Fig. 7). These results demonstrate that the presence of density drops across the MLDs can significantly reduce the size of V_s drops required to explain the amplitude of the observed signals, and that the relative contributions from V_s and density reductions are difficult to determine without additional constraints.

3 Inferring the origins of MLDs

3.1 Possible origins of MLDs

Previous studies have proposed many different physical mechanisms for MLDs, which can be broadly divided into four categories: (1) changes in composition, which includes the appearance of hydrous minerals (e.g., Rader et al., 2015; Selway et al., 2015; Krueger et al., 2021; Fu et al., 2022), and the decrease in depletion level (magnesium number Mg#; e.g., Yuan & Romanowicz, 2010), (2) the onset of partial melt (e.g., Thybo, 2006), (3) the onset of elastically-accommodated grain-boundary sliding , which can be due to increasing temperature or water content (e.g., Karato et al., 2015), and (4) changes in seismic anisotropy, which is usually attributed to the lattice-preferred orientaion (LPO) of olivine in unaltered peridotite (e.g., Yuan & Romanowicz, 2010; Ford et al., 2016; Yang et al., 2023). We prefer changes in composition and the presence of partial melts as the causes of our observed MLDs because they can generate significant azimuthal-invariant velocity drops in the mantle lithosphere (e.g., Chantel et al., 2016; Saha et al., 2018; Saha & Dasgupta, 2019). We will focus on models with compositional changes and partial melts in the coming sections and discuss other possible origins of MLDs in Section 4.5.

3.2 Mantle metasomatism and MLDs

One of the most commonly invoked physical mechanisms for MLDs is the presence of significant volumes of volatile-bearing phases (e.g., amphiboles and micas) with low velocities and possibly also low densities in the cratonic mantle lithosphere (e.g., Selway et al., 2015; Aulbach et al., 2017; Krueger et al., 2021), which are generated through metasomatic reactions between depleted peridotite and volatile-rich metasomatic reagents likely of slab origins. A series of recent experiments systematically explored the stability of metasomatic minerals and partial melts in the cratonic mantle lithosphere fluxed with different metasomatic reagents and the size of the resulting velocity drops (Saha et al., 2018; Saha & Dasgupta, 2019; Saha et al., 2021). Among different scenarios discussed by these studies, the reaction between depleted peridotite and CO_2-H_2O-rich siliceous melts causes the greatest amount of V_s drop (up to 6%) due to the precipitation of hydrous minerals (Saha et al., 2018), which is similar to our estimated V_s reductions across the MLDs beneath the two stations (2–9 %; Figs. 3, 4, 6, and 7). In addition, the presence of trace amounts of carbonate melt at temperatures above the magnesite stability field could further reduce the bulk V_s (Saha et al., 2018). Moreover, Both RSSD and ECSD are located close to the boundaries of Archean cratons (Figs. 1b and c), where volatile-rich melts from ancient subducting slabs likely percolated through and reacted with the original depleted cratonic mantle lithosphere. Specifically, RSSD is located on the Black Hills of South Dakota, where alkalic and carbonatitic magmas were intruded during the Cenozoic (Duke, 2009). These relatively recent magmatisms likely strongly altered the mantle lithosphere beneath RSSD, causing the overall stronger MLDs beneath it than ECSD (Figs. 3, 4, 6, and 7). We thus test if this melt-assisted metasomatism model could explain our MLD observations.

Fig. 8 shows the final equilibrium pressures and temperatures of xenoliths from the Eocene Homestead and Williams diatremes (Fig. 1c). We assume that these xenoliths are representative of the Wyoming craton, but may be less representative of the mantle lithosphere beneath the southwestern Superior province. Nonetheless, due to the great area of the Superior province and the scarcity of mantle xenoliths, the two sites are likely still among the sites closest to ECSD. For comparison, xenoliths from stable cratons (Slave, Kaapvaal, and Siberia; See Figure Caption for references) are also shown. Steady-state geotherms are calculated using the methods outlined in Rudnick et al. (1998) (see Table S1 for all input parameters). These geotherms assume a surface heat flow of 45 mW m^{-2}, which is representative of local heat flow measurements Blackwell et al. (2011) as well as global Archean cratons (Artemieva, 2009). Both the Homestead and Williams xenoliths plot at higher temperatures compared to the stable craton data, suggesting an elevated geotherm beneath the Wyoming craton compared to other cratons (Note that all P-T data in Fig. 8 utilize the thermobarometer from Brey and Köhler (1990) to minimize inherent artefacts of different thermobarometers when their results are compared (cf. Chin et al. (2012)).) Besides, the Wyoming-craton xenoliths are largely from shallower depths than the ones from other stable cratons, indicating possible lithospheric thinning, metasomatism, and hydration thought to be associated with the Laramide Orogeny (Currie & Beaumont, 2011; Carlson et al., 2004). Chin et al. (2021) also showed that pyroxene water contents of the Homestead and Williams xenoliths are elevated compared to other cratonic peridotites. Specifically, the Homestead and Williams xenoliths approach or overlap the hydration state of peridotite samples from beneath the Colorado Plateau (Chin et al., 2021), a craton-like lithosphere which was directly in the path of the Laramide flat slab and is thought to have been significantly re-hydrated by it (Li et al., 2008).

Fluxing of the Wyoming-craton lithosphere by CO2-H2O-rich siliceous melts, presumably of Laramide flat slab origin, may have resulted in substantial deposition of hydrous minerals (phlogopite, amphiboles) and carbonate minerals (magnesite) and even left behind "frozen" carbonated melt at certain depth ranges of the mantle lithosphere. Indeed, phlogopite is present in the Homestead xenoliths (Hearn Jr, 2004), although it is absent in the Williams xenoliths. The Homestead xenoliths were also found to contain more hydrous pyroxenes compared to the Williams xenoliths (Chin et al., 2021). To determine the stability depth ranges of these phases beneath the Wyoming craton and their relations with our observed MLDs, we compare the xenolith P-T data, reference geotherms, and experimental P-T conditions of hydrous phases in depleted peridotite fluxed by variable amounts of CO_2-H_2O-rich siliceous melts reported in Saha et al. (2018). The comparison shows that amphibole is stable in the range shallower than $\sim$110 km given the possible geotherms (Fig. 8), suggesting that MLD1 beneath the two stations might be caused by the presence of amphibole in 90–110 km, whereas MLD2 is unlikely to be associated with amphibole. In contrast, phlogopite is shown to be stable down to at least 130 km and thus could contribute to reducing the seismic velocities below MLD1. At greater depths, the solidus, which coincides with the stability boundary between magnesite and carbonated melt (Saha et al., 2018), intersects the geotherms at 110–120 km depth (Fig. 8), suggesting that the minimum stable depth of carbonated melt can be as shallow as 110 km, which coincides with the depth range of the MLD2 beneath the two stations (Fig. 8). In addition, the decomposition of amphibole at $\sim$110 km depth could also cause hydrous melting around the depth. Given the strong effect of small amounts of partial melts on V_s (Chantel et al., 2016), the onset of carbonated and hydrous melt could be the main cause of the MLD2 beneath the two stations.

3.3 "Melt-percolation barrier" model

Based on our seismic observations and thermal-chemical model, we propose a "Melt-percolation barrier" model to explain the MLDs beneath the two stations (Fig. 9). During a metasomatism event (e.g., the Laramide orogeny), CO_2-H_2O-rich siliceous melts, which are possibly released by a subducting slab beneath the cratonic lithosphere, percolated upward through the lithospheric mantle and started reacting with the peridotite to form phlogopite once they reached its stability field (Fig. 9). The reaction consumed the melts and may also have hindered their further ascent by creating networks of phlogopite-rich veins and sills, which have been observed in mantle xenoliths from the Wyoming craton (e.g., Carlson et al., 2004; Hearn Jr, 2004). A predominantly horizontal extension of the veins and sills can cause an increase in radial anisotropy and thus contribute to our observed MLD signals (Section 2.3.4 L. N. Hansen et al., 2021). If sufficient melts are injected into the mantle lithosphere, the melts will migrate further upward into the amphibole-stable zone (<110 km), and the formation of amphiboles will further consume the melts and impede their upward migration (Fig. 9). The result of this process is a melt-depletion front (equivalent to a metasomatism front) slightly above the lower boundary of the amphibole stability zone, which defines MLD1 below the two stations (Fig. 9). Although carbonated melts might have been stable at shallower depths due to a hotter geotherm during the metasomatism event, they are likely only stable below 110–120 km depth beneath the two stations today, which, together with possible hydrous melt caused by the decomposition of amphibole, defines MLD2 (Fig. 9).

The "Melt-percolation barrier model" explains two of our key seismic observations. First, the model predicts similar MLD1 and MLD2 depths given similar geotherms, which is consistent with the similar MLD depths observed for the two stations (Figs. 1, 3, and 4). The model can also explain the slightly deeper (∼10 km) MLD2 beneath ECSD than RSSD (Figs. 1, 3, and 4), which could be due to the colder geotherm beneath the southwestern Superior province causing a greater melt-onset depth. A remaining question is what controls the layer thickness between MLD1, i.e., the metasomatism front, and the lower boundary of the amphibole stability field, which appears to be ∼20 km beneath both stations despite the differences in temperature and melt supply between the two regions (Fig. 8). We speculate that the thickness is determined by the rates of metasomatic reaction and melt diffusion, although a quantitative assessment requires numerical simulations of the behaviors of reactive melts in the mantle lithosphere using realistic parameters, which is beyond the scope of this paper. Second, the metasomatic minerals generated by the melt-peridotite reactions are less dense and may cause radial anisotropy by forming horizontally oriented veins and sills, which will reduce the amount of isotropic V_s drops required to explain our observed MLD signals (Figs. 6 and 7) and thus render our results more consistent with previous results obtained using other methods (e.g., Krueger et al., 2021). The stronger MLD1 beneath RSSD can also be explained by a more abundant melt supply below the Wyoming craton during the Laramide period as evidenced by the widespread alkalic and carbonititic magmatism in the area (Duke, 2009), which likely deposited a greater volume of metasomatic minerals below MLD1 beneath RSSD and thus caused stronger isotropic V_s, density, and anisotropy contrasts (Figs. 6 and 7).

3.4 Metasomatic reagents: melts vs aqueous fluids

In addition to CO_2-H_2O-rich siliceous melts, aqueous fluids rich in CO_2 could also cause metasomatism of the mantle lithosphere (Saha & Dasgupta, 2019). Whereas the introduction of melts enriches the depleted peridotite with both volatiles and incompatible elements (e.g., Na and K), the infiltration of aqueous fluids only increases the volatile contents in the system (Table 1 in Saha & Dasgupta, 2019). This key difference causes distinct resulting phase assemblages for the two reagents, with melts generally favoring the deposition of metasomatic minerals (e.g., amphiboles and phlogopite) and fluids favoring the formation of melts (Saha & Dasgupta, 2019). We have chosen to use the phase equilibrium data from Saha et al. (2018) measured for melt-assisted metasomatism primarily because the resulting solid assemblage produces greater V_s drops (up to ∼6 %) due to its greater hydrous-phase content compared to the V_s drops produced by fluid-assisted metasomatism reported in Saha and Dasgupta (2019) (below 3 %). Nonetheless, the V_s drops reported in both studies are estimated without including the effects of melts despite clear evidence for the presence of up to 6 % of melts in many of their resulting phase assemblages (Table 2 in Saha & Dasgupta, 2019). Given the strong influence of melts on bulk V_s (Chantel et al., 2016) and the fact that fluid-assisted metasomatism stabilizes greater amounts of melt at lower temperatures (Saha & Dasgupta, 2019), the V_s reductions caused by fluid-assisted metasomatism could be comparable or even greater than the melt-assisted case if the V_s-reducing effects of melts are accounted for.

In the case of fluid-assisted metasomatism (i.e., no enrichment of incompatible elements), the stability fields of the hydrous phases are greatly reduced due to the low alkaline-water ratio (Saha & Dasgupta, 2019; Saha et al., 2021). Specifically, phlogopite decomposes and generates hydrous partial melts at $\sim$1000 °C and $\sim$3.5 GPa (Fig. 4 in Saha and Dasgupta (2019)), a P-T condition generally consistent with the geotherm of the Wyoming craton at the depth of our MLD2 (Fig. 8). MLD2 could thus originate from partial melting caused by the decomposition of phlogopite in the case of fluid-assisted metasomatism. Another important hydrous mineral, amphibole, was shown to be unstable in the P-T range tested in Saha and Dasgupta (2019) (2–4 GPa and 850–1150 °C). Nonetheless, because the stability of hydrous minerals is highly sensitive to the alkaline-water ratio (Saha & Dasgupta, 2019; Saha et al., 2021), there likely exists a mixture of incompatible elements and water that cause amphibole and phlogopite to decompose at the P-T conditions of our MLD1 and MLD2, respectively. In this case, MLD1 is caused by the initiation of partial melt due to the decomposition of amphibole, and MLD2 by a significant increase in the melt content due to the decomposition of phlogopite (Fig. S1). The mantle lithosphere above MLD1 contains small volumes of the two hydrous phases, which are insufficient to generate significant velocity drops (Fig. S1).

The scenario with fluids as the metasomatic reagents discussed above requires smaller volumes of hydrous minerals compared to the case with melts as the reagents and thus may be more consistent with mantle-xenolith evidence. Nonetheless, given the sparse and potentially biased sampling of mantle xenoliths, a relatively thin ($\sim$20 km; Fig. 8) and laterally intermittent layer with significant volumes of hydrous minerals could remain largely unsampled by xenoliths (Section 4.3). Because both the presence of hydrous minerals and partial melts could explain the seismic signature of MLD1 beneath the two stations, our observations are insufficient to determine its origin. On the other hand, electric-conductivity structure constrained using magnetotellurics could potentially distinguish between the two models because melts are much more potent in increasing the conductivity of the medium compared to hydrous minerals. Although we cannot uniquely determine the metasomatic reagents responsible for the two MLDs, we have shown that mantle metasomatism can generate two MLDs at the observed depths. The significant azimuthal-invariant velocity drops at the two MLDs also suggest mantle metasomatism as their most probable origin.

4 Discussions

4.1 Do MLDs exist beneath the central US?

Among different seismic imaging techniques, the SRF technique is most widely used for imaging MLDs because the S-to-P conversions at mantle interfaces arrive before direct S and thus are free from the interference of crustal multiple-reflection phases. Using the SRF technique, a series of papers have identified one or multiple MLDs beneath a significant portion of the central US (e.g., Abt et al., 2010; Hopper & Fischer, 2015, 2018). Nonetheless, a recent study processed the S-to-P phases using a direct stacking approach and found no evidence for MLDs beneath the central US (Kind et al., 2020). The authors thus claimed that the MLDs beneath the central US found by previous SRF studies are Moho sidelobes generated by the deconvolution procedure (Kind et al., 2020). This controversy highlights the challenges in characterizing MLDs seismically and thus calls for independent seismic observations to address this issue. Here, using the SH-reverberation method, we present strong evidence for the presence of MLDs beneath two stations separated by $\sim$600 km in the central US. Moreover, the depths of the two MLDs beneath RSSD agree well with the ones found by Krueger et al. (2021) using the SRF technique. These findings support the presence of MLDs beneath at least parts of the central US. We also note that the discrepancy between different studies using S-to-P phases to study MLDs is not limited to that between Kind et al. (2020) and previous SRF studies; another example is the disagreement between EFD18, which suggested an MLD at $\sim$60 km depth beneath RSSD, and Krueger et al. (2021), which showed two MLDs at $\sim$85 km and ∼110 km depth beneath the station. These discrepancies suggest that nuances in the processing of S-to-P phases may have major impacts on the results.

4.2 Contributions from anisotropy and density variations

Assuming that our observed MLD signals are caused only by isotropic V_s drops, the minimum amount of isotropic V_s reductions required to produce the signals (assuming a zero gradient-zone thickness) is 4–9 % (Figs. 3 and 4), which is significantly greater than the 1–4 % estimated by Krueger et al. (2021) for global cratons using SRFs. Specifically, at RSSD, where Krueger et al. (2021) found similar depths for the two MLDs as we observe here, their study estimated ∼4 % isotropic V_s drops across both MLDs in contrast to our estimates of ∼7 % and ∼8 % for MLD1 and MLD2, respectively (Fig. 3). One way to reconcile our results and previous SRF results is assuming that the drops in isotropic V_s are accompanied by increases in radial anisotropy and density reductions, which can significantly reduce the amount of isotropic-V_s reductions required to explain our observed signals (Figs. 6 and 7). Specifically, scaling factors $c = 2.0$ for the radial-anisotropy case and $c = 1.0$ for the density-reduction case can both approximately halve the amount of isotropic-V_s reduction in the preferred models for RSSD (Figs, 6a and 7a), rendering the results generally consistent with those from Krueger et al. (2021). The amount of radial-anisotropy increase and density decrease required to achieve similar degrees of isotropic V_s reductions across MLDs will be further reduced if both parameters are allowed to vary. Increases in radial anisotropy and density reductions across MLDs are also consistent with a metasomatic origin of MLDs because the hydrous phases deposited by metasomatic reactions can cause up to a ∼3 % density drop across a metamsomatic front (Saha et al., 2018), and a high concentration of horizontally oriented veins and sills rich in hydrous phases can cause an increase in radial anisotropy.

Despite the ability of the models with radial-anisotropy and density variations to reconcile our results with previous SRF ones, they also present their own challenges: Our preferred radially anisotropic models show significantly greater variation in ξ with depth than previous tomography models (Fig. 6), and density inversions could destabilize the lithosphere (see Section 4.4 for detailed discussions). Addressing these issues requires a better understanding of how radial anisotropy and density vary with depth in the lithosphere, which cannot be achieved with the SH-reverberation technique alone because the reflection phases are only sensitive to gradients in medium properties and a trade-off exists between different model parameters in explaining the phase amplitudes (Figs. 6 and 7). An obvious solution is to combine multiple types of observations, e.g., SH reverberations, SRFs, and surface waves. We will discuss the sensitivities, advantages, and disadvantages of common methods for studying MLDs in detail in Section 4.6.

4.3 Reconciling with geochemistry: compositional heterogeneity?

The metasomatic origin of MLDs requires enrichment of the depleted cratonic mantle lithosphere by volatile and incompatible elements, which apparently contradicts mantle-xenolith evidence suggesting a cratonic lithosphere highly depleted in the two components (e.g., Lee et al., 2011). For example, Saha et al. (2021) argued that based on xenolith evidence, the average cratonic peridotite is too depleted in incompatible elements to stabilize enough hydrous minerals to explain the full spectrum of V_s drops observed for MLDs. To reconcile the metasomatic origin of MLDs with geochemical evidence, we propose that the cratonic mantle lithosphere is probably highly heterogeneous in composition, with some domains significantly refertilized by volatile and incompatible elements through metasomatism (Fig. 10) and the rest remaining largely intact (Fig. 10). The enriched domains may be mostly located near the craton boundaries, where fluids and melts released by past subducting slabs could have metasomatized the mantle lithosphere and generated strong MLDs (Fig. 10). This model is consistent with stronger MLDs observed near craton boundaries compared to craton interiors globally (Krueger et al., 2021). Because the enriched domains are likely spatially intermittent, they are probably less well-sampled by mantle xenoliths, which are also sparsely distributed. Furthermore, some unknown mechanisms may cause kimberlite eruptions, the primary host for mantle xenoliths in cratons, to preferentially entrain mantle rocks that are not metasomatized. A tentative model is that kimberlite eruptions, the main host of cratonic mantle xenoliths, may happen in different domains from mantle metasomatism because the two processes have dramatically different time scales: kimberlite usually erupt very rapidly, whereas mantle metasomatism requires extended periods of contact between depleted peridotite and metasomatic reagents to allow for complete reactions. Given the scarcity of mantle-xenolith samples, methods capable of better characterizing the true spatial extents of mantle metasomatism are required to test the hypothesis of compositional heterogeneity beneath cratons. Our results suggest that the detection of MLDs may be a reliable indicator for the presence of mantle metasomatism beneath the station, which provides a promising method to explore compositional heterogeneity beneath cratons.

4.4 Implications on craton stability

Although cratons have generally remained stable since their formations in the Precambrian, the reactivation and even destruction of cratons during the Phanerozoic have also been extensively documented (e.g., the destruction of the eastern North China craton; Zhu & Xu, 2019, and references therein.). MLDs caused by volatile-bearing phases and melts may facilitate the modification of the cratonic lithosphere in two ways. First, the presence of significant volumes of hydrous minerals and trace amounts of melts can rheologically weaken the mantle lithosphere and thus facilitate its modification by mantle convection (e.g, Wang et al., 2023). We note that a recent petrological study found that whereas volatile-rich melts significantly weaken the upper mantle, the presence of hydrous minerals up to 25 vol.% do not (Tommasi et al., 2017). These results suggest that trace amounts of melts within the cratonic mantle lithosphere may play a critical role in promoting its destruction. Second, the presence of significant volumes of hydrous minerals in a depth range in the mantle lithosphere can reduce its density compared to the materials above it, causing gravitational instability. This scenario is similar to the case where an eclogitized lower crust is denser than the underlying mantle and thus could cause its delamination (Jull & Kelemen, 2001). Although our waveform modeling suggests that the MLDs beneath RSSD and ECSD may represent density reductions with depth (Fig. 7), these gravitationally unstable structures do not seem to have destabilized the two cratons, probably because the high viscosity of the cold cratonic mantle lithosphere inhibits the process (Jull & Kelemen, 2001). Nonetheless, in the event of the cratons reheated by the arrival of a plume, these gravitationally unstable structures could destabilize the mantle lithosphere with a reduced viscosity and thus destroy the cratons. In summary, mantle metasomatism could plant the seeds for future craton reactivation and destruction.

4.5 Other origins of MLDs

Our metasomatism model for the MLDs beneath the two stations can be regarded as a combination of changes in composition (hydrous phases), melt content (carbonated melt), and anisotropy (sub-horizontal veins and sills rich in hydrous phases), although the origin of the anisotropy in our model is not olivine LPO as suggested by most previous studies. In addition to these three factors, onsets of EAGBS may also contribute to our observed MLD signals because the hydration of the lower lithosphere (Chin & Palin, 2022) by metasomatism could have enabled EAGBS (Fig. 10), causing a few percent of velocity drop and thus reducing the amount of hydrous phases and melts required to explain our observed MLD signals (Karato et al., 2015; Saha et al., 2021). Nonetheless, a recent experimental study rejected EAGBS as a possible cause of sharp velocity drops in the upper mantle (Cline II et al., 2018), highlighting the controversy over this mechanism.

Abrupt changes in olivine LPO with depth, which are likely associated with deformations during craton formation, could also generate seismically detectable MLDs (Fig. 10). The evidence for this physical mechanism is scarce because observing its hallmark, an azimuthal variation in scattered-phase amplitude and polarity (e.g., Figure 3 in Ford et al., 2016), requires reasonably good back-azimuth coverage of the events, which is difficult to achieve for both SRF and SH-reverberation techniques, the two most commonly used methods for studying MLDs (See Section 4.6). So far, only a few PRF studies have reported contrasts in azimuthal anisotropy across MLDs (e.g., Wirth & Long, 2014; Ford et al., 2016), which are probably due to sharp changes in olivine LPO with depth. Nonetheless, the significant variation of azimuthal anisotropy with depth beneath cratons reported by previous tomography studies (e.g., Yuan & Romanowicz, 2010) suggests that changes in olivine LPO may play a more important role in causing MLDs than currently understood.

Some previous studies attempted to find a universal physical model for the MLDs observed globally (e.g., EAGBS proposed by Karato et al., 2015), yet recent seismological investigations are painting an increasingly complicated picture of MLDs, suggesting likely diverse origins of MLDs in different regions. For example, the continental-scale study of Liu and Shearer (2021) found highly variable MLD depths and amplitudes beneath the central US, with some regions underlain by multiple MLDs, and the global-scale study of Krueger et al. (2021) detected MLDs only beneath ∼50 % of the long-running stations and found that the MLD amplitudes generally decrease from craton edges to interiors. These findings suggest that MLDs beneath different areas probably have distinct properties (e.g., depth, amplitude, and azimuthal variation) and thus may have different origins. This complexity is ultimately caused by the long and complicated histories of cratons (Fig. 10). Therefore, finding a universal physical model for MLDs may be unrealistic. Instead, future studies should focus on uncovering the origins of MLDs on a case-by-case basis, which requires more detailed investigations and synthesis of knowledge across different disciplines.

4.6 Methods for studying MLDs and future directions

So far, most of the observational constraints of MLDs come from scattered-phase imaging methods, with different methods having distinct sensitivities and limitations. Although PRFs have been widely used for studying crustal and mantle-transition-zone structures, they are not commonly used for studying MLDs due to interference from crustal reverberations (Figure 1d in Liu & Shearer, 2021). In contrast, SRFs are free from the interference caused by crustal reverberations and thus are widely used for studying MLDs. In addition to the well-known sensitivity of the S-to-P amplitude in SRFs to isotropic V_s changes, the amplitude is also affected by changes in radial anisotropy (e.g., extended Figure 6 in Hua et al., 2023), with the dependence involving both anisotropy amplitude and Kawakatsu's fifth parameter (η_κ; Kawakatsu, 2018). Despite the broad application of the SRF technique to studying MLDs, it also has three well-known limitations: First, the depth resolution is limited due to the low frequency range of teleseismic S waves and the small temporal separations between the S-to-P phases generated at different interfaces (Figure 1e in Liu & Shearer, 2021). Second, the S-to-P conversion points are usually far from the recording station (∼140 km for an interface at 100 km depth) and thus may cause events from different back azimuths to sample different structures (e.g., RSSD1 and RSSD2 in Figure 6b of Krueger et al., 2021), which could degrade the result if the events from different back azimuths are averaged. Moreover, the shape of the SRF scattering kernel also limits its use in imaging interfaces with strong lateral changes (Hua et al., 2020). Third, to avoid the interference from other global phases, SRF studies typically only use events within a relatively narrow distance range (e.g., 65–80° in Krueger et al., 2021), which limits the number of available events.

Compared to receiver-function methods, the SH-reverberation technique is less susceptible to interference from crustal reverberations than the PRF technique and has better depth resolution than the SRF technique (Figure 1c in Liu & Shearer, 2021), rendering it a powerful tool for imaging MLDs and other lithospheric discontinuities. As shown in Section 2.3.2, the SH-reverberation amplitude is sensitive to changes in isotropic V_s, radial anisotropy, and density, and the relative contributions from the three factors cannot be determined without independent constraints (Figs. 6 and 7). Similar to the SRF method, the SH-reverberation method also has limitations in event availability: Deep events are often used to avoid the ambiguity between source- and receiver-side scatterers (Fig. 2a) and the events in 65–85° are sometimes excluded to avoid interference from *ScS*.

Given the complementary sensitivities of different scattered-phase imaging methods, an obvious future direction is combining different types of observations to better constrain the physical-property changes across the MLDs. Specifically, integrating SRF and SH-reverberation observations may hold the potential to independently constrain the changes in isotropic V_s, radial anisotropy, and density across MLDs beneath long-running stations where both methods provide high-quality observations (e.g., RSSD and ECSD). For example, at RSSD, the significantly higher isotropic V_s drops required to fully explain the MLD signals in SH-reverberation observations compared to SRF observations suggest significant contributions from radial-anisotropy or density contrasts (Section 4.2). Nonetheless, we caution that combining different types of observations at a single station requires the assumption that the structure beneath the station can be approximated with a 1D model, which may not be valid in some cases as evidenced by the discrepancy between the SRF stacks for two different back-azimuth windows at RSSD (Krueger et al., 2021). In addition to multiple scattered-phase observations, surface-wave observations can also be incorporated to better constrain the absolute velocities in the mantle lithosphere (Eilon et al., 2018). Specifically, we note that the current tomography models of the contiguous US seem to disagree on the trend of radial-anisotropy variation in the lithosphere (Fig. 6), i.e., if the maximum of radial-anisotropy is located in the crust or the mantle lithosphere. This issue is worth further investigation given the potential for radial-anisotropy contrasts to cause MLDs (Figs. 5a and 6). Moreover, magnetotellurics (MT) may also provide valuable information on the origins of MLDs due to its sensitivity to melts, which can be used to distinguish between MLD models with hydrous phases and melts as the cause for velocity reductions (Section 3.4). Although MT has been applied to studying the LAB (e.g., Blatter et al., 2022), its application in studying MLDs is still limited and thus could be further explored in the future. Lastly, the current understanding of MLDs is severely restricted by data availability because both the SRF and SH-reverberation methods require data from long-running stations, which are much scarcer in cratons than in tectonically active regions (e.g., west coast of the US; Figure 5g in Liu & Shearer, 2021). This lack of station coverage is especially acute given the growing body of evidence suggesting that the internal structures of cratons may be as complicated as tectonically active regions (Krueger et al., 2021; Liu & Shearer, 2021). Although increasing the number of permanent seismic stations in cratons may not be feasible in the short term due to a lack of resources, keeping the current global and regional seismic networks (e.g, Global Seismographic Network), which provide crucial station coverage for many cratons globally, operative is critical for continuing accumulating the seismic data required for better understanding the structure and evolution of cratons.

5 Conclusions

We detect two distinct MLDs at ~ 89 (MLD1) and ~ 115 (MLD2) km depth beneath the eastern Wyoming craton and the southwestern Superior craton with 2–10 % isotropic V_s drops, depending on the contributions from contrasts in density and radial anisotropy. MLD1 and MLD2 are probably caused by the appearance of significant volumes of hydrous minerals and the onset of carbonated partial melting, respectively. The hydrous minerals and melts are likely products of melt-assisted metasomatism of the mantle lithosphere. Our results suggest that metasomatism is probably the cause for the strong MLDs observed globally near craton boundaries, where the mantle lithosphere could have been intensely metasomatized by fluids and melts released by past subducting slabs. The apparent contradiction between the metasomatism origin of MLDs and mantle-xenolith evidence suggests significant compositional heterogeneity in cratonic mantle lithospheres.

Conflict of interest

The authors declare no conflicts of interest relevant to this study.

Open Research Section

The seismic waveform data are publicly available through the Seismological Facility for the Advancement of Geoscience (SAGE) data management center `https://ds.iris.edu/mda/` by the network code "IU" (RSSD) and "US" (ECSD). The heat-flow data are publicly available through the National Geothermal Data System (NGDS) `http://geothermal.smu.edu/gtda/`. The open-source software *Aniplane.jl* is freely available at `https://github.com/tianzeliu/Aniplane.jl.git`. Some of the figures are created using the Generic Mapping Tools (GMT; Wessel et al., 2019).

Acknowledgments

We thank Vera Schulte-Pelkum for her advice on seismic anisotropy. We thank Zach Eilon for sharing the velocity model EFD18. We thank Hongzhan Fei for insightful discussions about mineral physics. T.L. is supported by the National Science Foundation (NSF) grant EAR 2123529.

References

Abt, D. L., Fischer, K. M., French, S. W., Ford, H. A., Yuan, H., & Romanowicz, B. (2010). North american lithospheric discontinuity structure imaged by ps and sp receiver functions. *Journal of Geophysical Research: Solid Earth*, *115*(B9).

Artemieva, I. M. (2009). The continental lithosphere: Reconciling thermal, seismic, and petrologic data. *Lithos*, *109*(1-2), 23–46.

Aulbach, S., Griffin, W. L., Pearson, N. J., O'Reilly, S. Y., & Doyle, B. J. (2007). Lithosphere formation in the central slave craton (canada): plume subcretion or lithosphere accretion? *Contributions to Mineralogy and Petrology*, *154*, 409–427.

Aulbach, S., Massuyeau, M., & Gaillard, F. (2017). Origins of cratonic mantle discontinuities: A view from petrology, geochemistry and thermodynamic models. *Lithos*, *268*, 364–382.

Bell, D. R., Gregoire, M., Grove, T., Chatterjee, N., Carlson, R., & Buseck, P. (2005). Silica and volatile-element metasomatism of archean mantle: a xenolith-scale example from the kaapvaal craton. *Contributions to Mineralogy and Petrology*, *150*, 251–267.

Blackwell, D., Richards, M., Frone, Z., Batir, J., Ruzo, A., Dingwall, R., & Williams, M. (2011). *Temperature-at-depth maps for the conterminous us and geothermal* *resource estimates* (Tech. Rep.). Southern Methodist University Geothermal Laboratory, Dallas, TX (United States).

Blatter, D., Naif, S., Key, K., & Ray, A. (2022). A plume origin for hydrous melt at the lithosphere–asthenosphere boundary. *Nature*, *604*(7906), 491–494.

Brey, G. P., & Köhler, T. (1990). Geothermobarometry in four-phase lherzolites ii. new thermobarometers, and practical assessment of existing thermobarometers. *Journal of Petrology*, *31*(6), 1353–1378.

Carlson, R. W., Irving, A. J., Schulze, D. J., & Hearn Jr, B. C. (2004). Timing of precambrian melt depletion and phanerozoic refertilization events in the lithospheric mantle of the wyoming craton and adjacent central plains orogen. *Lithos*, *77*(1-4), 453–472.

Chantel, J., Manthilake, G., Andrault, D., Novella, D., Yu, T., & Wang, Y. (2016). Experimental evidence supports mantle partial melting in the asthenosphere. *Science advances*, *2*(5), e1600246.

Chin, E. J., Chilson-Parks, B., Boneh, Y., Hirth, G., Saal, A. E., Hearn, B. C., & Hauri, E. H. (2021). The peridotite deformation cycle in cratons and the deep impact of subduction. *Tectonophysics*, *817*, 229029.

Chin, E. J., Lee, C.-T. A., Luffi, P., & Tice, M. (2012). Deep lithospheric thickening and refertilization beneath continental arcs: Case study of the p, t and compositional evolution of peridotite xenoliths from the sierra nevada, california. *Journal of Petrology*, *53*(3), 477–511.

Chin, E. J., & Palin, R. M. (2022). Water storage in cratonic mantle. *Terra Nova*, *34*(5), 369–380.

Cline II, C., Faul, U., David, E., Berry, A., & Jackson, I. (2018). Redox-influenced seismic properties of upper-mantle olivine. *Nature*, *555*(7696), 355–358.

Crampin, S. (1981). A review of wave motion in anisotropic and cracked elastic-media. *Wave motion*, *3*(4), 343–391.

Currie, C. A., & Beaumont, C. (2011). Are diamond-bearing cretaceous kimberlites related to low-angle subduction beneath western north america? *Earth and Planetary Science Letters*, *303*(1-2), 59–70.

Dalton, C. A., Ekström, G., & Dziewoński, A. M. (2008). The global attenuation structure of the upper mantle. *Journal of Geophysical Research: Solid Earth*, *113*(B9).

Downes, H., Macdonald, R., Upton, B. G., Cox, K. G., Bodinier, J.-L., Mason, P. R., ... Hearn Jr, B. C. (2004). Ultramafic xenoliths from the bearpaw mountains, montana, usa: Evidence for multiple metasomatic events in the lithospheric mantle beneath the wyoming craton. *Journal of Petrology*, *45*(8), 1631–1662.

Duke, G. I. (2009). Black hills–alberta carbonatite–kimberlite linear trend: Slab edge at depth? *Tectonophysics*, *464*(1-4), 186–194.

Eilon, Z., Fischer, K. M., & Dalton, C. A. (2018). An adaptive bayesian inversion for upper-mantle structure using surface waves and scattered body waves. *Geophysical Journal International*, *214*(1), 232–253.

Ford, H. A., Fischer, K. M., Abt, D. L., Rychert, C. A., & Elkins-Tanton, L. T. (2010). The lithosphere–asthenosphere boundary and cratonic lithospheric layering beneath australia from sp wave imaging. *Earth and Planetary Science Letters*, *300*(3-4), 299–310.

Ford, H. A., Long, M. D., & Wirth, E. A. (2016). Midlithospheric discontinuities and complex anisotropic layering in the mantle lithosphere beneath the wyoming and superior provinces. *Journal of Geophysical Research: Solid Earth*, *121*(9), 6675–6697.

Fu, H.-Y., Li, Z.-H., & Chen, L. (2022). Continental mid-lithosphere discontinuity: A water collector during craton evolution. *Geophysical Research Letters*, e2022GL101569.

Gibson, S. A., Malarkey, J., & Day, J. A. (2008). Melt depletion and enrichment beneath the western kaapvaal craton: evidence from finsch peridotite xenoliths. *Journal of Petrology*, *49*(10), 1817–1852.

Hacker, B. R., Kelemen, P. B., & Behn, M. D. (2015). Continental lower crust. *Annual Review of Earth and Planetary Sciences*, *43*, 167–205.

Hansen, L. N., Faccenda, M., & Warren, J. M. (2021). A review of mechanisms generating seismic anisotropy in the upper mantle. *Physics of the Earth and Planetary Interiors*, *313*, 106662.

Hansen, S. M., Dueker, K., & Schmandt, B. (2015). Thermal classification of lithospheric discontinuities beneath usarray. *Earth and Planetary Science Letters*, *431*, 36–47.

Hearn Jr, B. C. (2004). The homestead kimberlite, central montana, usa: mineralogy, xenocrysts, and upper-mantle xenoliths. *Lithos*, *77*(1-4), 473–491.

Hopper, E., & Fischer, K. M. (2015). The meaning of midlithospheric discontinuities: A case study in the northern us craton. *Geochemistry, Geophysics, Geosystems*, *16*(12), 4057–4083.

Hopper, E., & Fischer, K. M. (2018). The changing face of the lithosphere-asthenosphere boundary: Imaging continental scale patterns in upper mantle structure across the contiguous us with sp converted waves. *Geochemistry, Geophysics, Geosystems*, *19*(8), 2593–2614.

Hua, J., Fischer, K. M., Becker, T. W., Gazel, E., & Hirth, G. (2023). Asthenospheric low-velocity zone consistent with globally prevalent partial melting. *Nature Geoscience*, *16*(2), 175–181.

Hua, J., Fischer, K. M., Mancinelli, N. J., & Bao, T. (2020). Imaging with pre-stack migration based on sp scattering kernels. *Geophysical Journal International*, *220*(1), 428–449.

Ionov, D. A., Doucet, L. S., & Ashchepkov, I. V. (2010). Composition of the lithospheric mantle in the siberian craton: new constraints from fresh peridotites in the udachnaya-east kimberlite. *Journal of petrology*, *51*(11), 2177–2210.

Ionov, D. A., Shirey, S. B., Weis, D., & Brügmann, G. (2006). Os–hf–sr–nd isotope and pge systematics of spinel peridotite xenoliths from tok, se siberian craton: effects of pervasive metasomatism in shallow refractory mantle. *Earth and Planetary Science Letters*, *241*(1-2), 47–64.

Jull, M., & Kelemen, P. á. (2001). On the conditions for lower crustal convective instability. *Journal of Geophysical Research: Solid Earth*, *106*(B4), 6423–6446.

Karato, S.-i., Olugboji, T., & Park, J. (2015). Mechanisms and geologic significance of the mid-lithosphere discontinuity in the continents. *Nature Geoscience*, *8*(7), 509–514.

Katsura, T. (2022). A revised adiabatic temperature profile for the mantle. *Journal of Geophysical Research: Solid Earth*, *127*(2), e2021JB023562.

Katz, R. F., Spiegelman, M., & Langmuir, C. H. (2003). A new parameterization of hydrous mantle melting. *Geochemistry, Geophysics, Geosystems*, *4*(9).

Kawakatsu, H. (2016a). A new fifth parameter for transverse isotropy. *Geophysical Journal International*, *204*(1), 682–685.

Kawakatsu, H. (2016b). A new fifth parameter for transverse isotropy ii: Partial derivatives. *Geophysical Journal International*, *206*(1), 360–367.

Kawakatsu, H. (2018). A new fifth parameter for transverse isotropy iii: reflection and transmission coefficients. *Geophysical Journal International*, *213*(1), 426–433.

Kennett, B. (2009). *Seismic wave propagation in stratified media.* ANU E Press.

Kind, R., Mooney, W. D., & Yuan, X. (2020). New insights into the structural elements of the upper mantle beneath the contiguous united states from s-to-p converted seismic waves. *Geophysical Journal International*, *222*(1), 646–659.

Kopylova, M., & Caro, G. (2004). Mantle xenoliths from the southeastern slave craton: evidence for chemical zonation in a thick, cold lithosphere. *Journal of Petrology*, *45*(5), 1045–1067.

Krischer, L., Fichtner, A., Boehm, C., & Igel, H. (2018). Automated large-scale full seismic waveform inversion for north america and the north atlantic. *Journal of Geophysical Research: Solid Earth*, *123*(7), 5902–5928.

Krueger, H. E., Gama, I., & Fischer, K. M. (2021). Global patterns in cratonic mid-lithospheric discontinuities from sp receiver functions. *Geochemistry, Geophysics, Geosystems*, *22*(6), e2021GC009819.

Lee, C.-T. A., Luffi, P., & Chin, E. J. (2011). Building and destroying continental mantle. *Annual Review of Earth and Planetary Sciences*, *39*, 59–90.

Lei, W., Ruan, Y., Bozdağ, E., Peter, D., Lefebvre, M., Komatitsch, D., … Pugmire, D. (2020). Global adjoint tomography—model glad-m25. *Geophysical Journal International*, *223*(1), 1–21.

Li, Z.-X. A., Lee, C.-T. A., Peslier, A. H., Lenardic, A., & Mackwell, S. J. (2008). Water contents in mantle xenoliths from the colorado plateau and vicinity: Implications for the mantle rheology and hydration-induced thinning of continental lithosphere. *Journal of Geophysical Research: Solid Earth*, *113*(B9).

Liu, T., & Shearer, P. M. (2021). Complicated lithospheric structure beneath the contiguous us revealed by teleseismic s-reflections. *Journal of Geophysical Research: Solid Earth*, *126*(5), e2020JB021624.

Mancinelli, N. J., Fischer, K. M., & Dalton, C. A. (2017). How sharp is the cratonic lithosphere-asthenosphere transition? *Geophysical Research Letters*, *44*(20), 10–189.

Miller, M. S., & Eaton, D. W. (2010). Formation of cratonic mantle keels by arc accretion: Evidence from s receiver functions. *Geophysical Research Letters*, *37*(18).

Panning, M., & Romanowicz, B. (2006). A three-dimensional radially anisotropic model of shear velocity in the whole mantle. *Geophysical Journal International*, *167*(1), 361–379.

Pearson, D., Shirey, S., Carlson, R., Boyd, F. R., Pokhilenko, N., & Shimizu, N. (1995). Re-os, sm-nd, and rb-sr isotope evidence for thick archaean lithospheric mantle beneath the siberian craton modified by multistage metasomatism. *Geochimica et Cosmochimica Acta*, *59*(5), 959–977.

Porritt, R. W., Becker, T. W., Boschi, L., & Auer, L. (2021). Multiscale, radially anisotropic shear wave imaging of the mantle underneath the contiguous united states through joint inversion of usarray and global data sets. *Geophysical Journal International*, *226*(3), 1730–1746.

Rader, E., Emry, E., Schmerr, N., Frost, D., Cheng, C., Menard, J., … Geist, D. (2015). Characterization and petrological constraints of the midlithospheric discontinuity. *Geochemistry, Geophysics, Geosystems*, *16*(10), 3484–3504.

Rudnick, R. L., McDonough, W. F., & O'Connell, R. J. (1998). Thermal structure, thickness and composition of continental lithosphere. *Chemical Geology*, *145*(3-4), 395–411.

Saha, S., & Dasgupta, R. (2019). Phase relations of a depleted peridotite fluxed by a co2-h2o fluid—implications for the stability of partial melts versus volatile-bearing mineral phases in the cratonic mantle. *Journal of Geophysical Research: Solid Earth*, *124*(10), 10089–10106.

Saha, S., Dasgupta, R., & Tsuno, K. (2018). High pressure phase relations of a depleted peridotite fluxed by co2-h2o-bearing siliceous melts and the origin of mid-lithospheric discontinuity. *Geochemistry, Geophysics, Geosystems*, *19*(3), 595–620.

Saha, S., Peng, Y., Dasgupta, R., Mookherjee, M., & Fischer, K. M. (2021). Assessing the presence of volatile-bearing mineral phases in the cratonic mantle as a possible cause of mid-lithospheric discontinuities. *Earth and Planetary Science Letters*, *553*, 116602.

Savage, B., & Silver, P. G. (2008). Evidence for a compositional boundary within the lithospheric mantle beneath the kalahari craton from s receiver functions.

Earth and Planetary Science Letters, *272*(3-4), 600–609.

Schaeffer, A., & Lebedev, S. (2013). Global shear speed structure of the upper mantle and transition zone. *Geophysical Journal International*, *194*(1), 417–449.

Schulte-Pelkum, V., & Mahan, K. H. (2014). A method for mapping crustal deformation and anisotropy with receiver functions and first results from usarray. *Earth and Planetary Science Letters*, *402*, 221–233.

Selway, K., Ford, H., & Kelemen, P. (2015). The seismic mid-lithosphere discontinuity. *Earth and Planetary Science Letters*, *414*, 45–57.

Shearer, P. M., & Buehler, J. (2019). Imaging upper-mantle structure under usarray using long-period reflection seismology. *Journal of Geophysical Research: Solid Earth*, *124*(9), 9638–9652.

Simon, N. S., Carlson, R. W., Pearson, D. G., & Davies, G. R. (2007). The origin and evolution of the kaapvaal cratonic lithospheric mantle. *Journal of Petrology*, *48*(3), 589–625.

Sleep, N. H. (2005). Evolution of the continental lithosphere. *Annu. Rev. Earth Planet. Sci.*, *33*, 369–393.

Sodoudi, F., Yuan, X., Kind, R., Lebedev, S., Adam, J. M.-C., Kästle, E., & Tilmann, F. (2013). Seismic evidence for stratification in composition and anisotropic fabric within the thick lithosphere of kalahari craton. *Geochemistry, Geophysics, Geosystems*, *14*(12), 5393–5412.

Tharimena, S., Rychert, C., & Harmon, N. (2017). A unified continental thickness from seismology and diamonds suggests a melt-defined plate. *Science*, *357*(6351), 580–583.

Thybo, H. (2006). The heterogeneous upper mantle low velocity zone. *Tectonophysics*, *416*(1-4), 53–79.

Tommasi, A., Langone, A., Padrón-Navarta, J. A., Zanetti, A., & Vauchez, A. (2017). Hydrous melts weaken the mantle, crystallization of pargasite and phlogopite does not: Insights from a petrostructural study of the finero peridotites, southern alps. *Earth and Planetary Science Letters*, *477*, 59–72.

Wang, Y., Cao, Z., Peng, L., Liu, L., Chen, L., Lundstrom, C., … Yang, X. (2023). Secular craton evolution due to cyclic deformation of underlying dense mantle lithosphere. *Nature Geoscience*, 1–9.

Wessel, P., Luis, J., Uieda, L., Scharroo, R., Wobbe, F., Smith, W. H., & Tian, D. (2019). The generic mapping tools version 6. *Geochemistry, Geophysics, Geosystems*, *20*(11), 5556–5564.

Whitmeyer, S. J., & Karlstrom, K. E. (2007). Tectonic model for the proterozoic growth of north america. *Geosphere*, *3*(4), 220–259.

Wirth, E. A., & Long, M. D. (2014). A contrast in anisotropy across mid-lithospheric discontinuities beneath the central united states—a relic of craton formation. *Geology*, *42*(10), 851–854.

Wölbern, I., Rümpker, G., Link, K., & Sodoudi, F. (2012). Melt infiltration of the lower lithosphere beneath the tanzania craton and the albertine rift inferred from s receiver functions. *Geochemistry, Geophysics, Geosystems*, *13*(8).

Yang, H., Artemieva, I. M., & Thybo, H. (2023). The mid-lithospheric discontinuity caused by channel flow in proto-cratonic mantle. *Journal of Geophysical Research: Solid Earth*, e2022JB026202.

Yuan, H., French, S., Cupillard, P., & Romanowicz, B. (2014). Lithospheric expression of geological units in central and eastern north america from full waveform tomography. *Earth and Planetary Science Letters*, *402*, 176–186.

Yuan, H., & Romanowicz, B. (2010). Lithospheric layering in the north american craton. *Nature*, *466*(7310), 1063–1068.

Zhu, R., & Xu, Y. (2019). The subduction of the west pacific plate and the destruction of the north china craton. *Science China Earth Sciences*, *62*, 1340–1350.

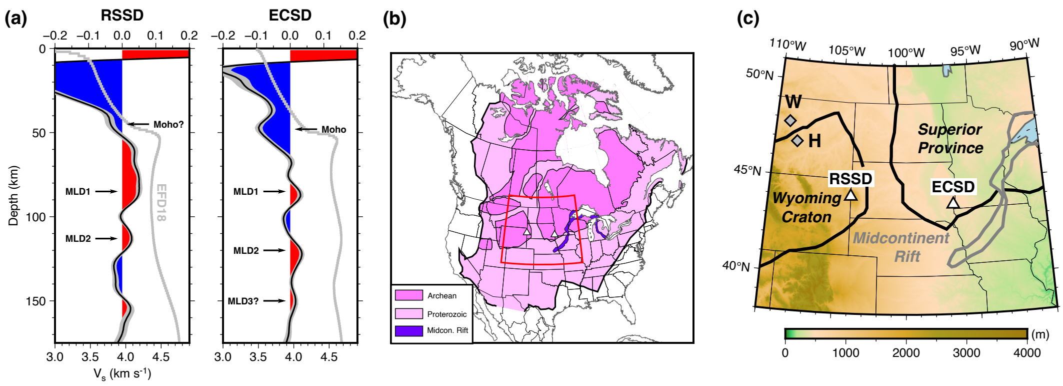

Figure 1. Summary of the seismic observations, station and xenolith locations, and key geological boundaries. (a) Depth-domain SH-reverberation stacks produced using all available events for RSSD (left) and ECSD (right). Blue and red denote impedance increases and decreases with depth, respectively. Gray curve: V_s models from EF18. (b) Locations of RSSD and ECSD and boundaries of Archean (dark pink) and Proterozoic (light pink) terrains of North America. The Midcontinent Rift is shown in purple. Red box: boundary of the close-in map in (c). (c) Close-in map showing the location of the stations and Homestead (H) and Williams (W) mantle xenoliths. The terrain boundaries in (b) and (c) are simplified from Whitmeyer and Karlstrom (2007).

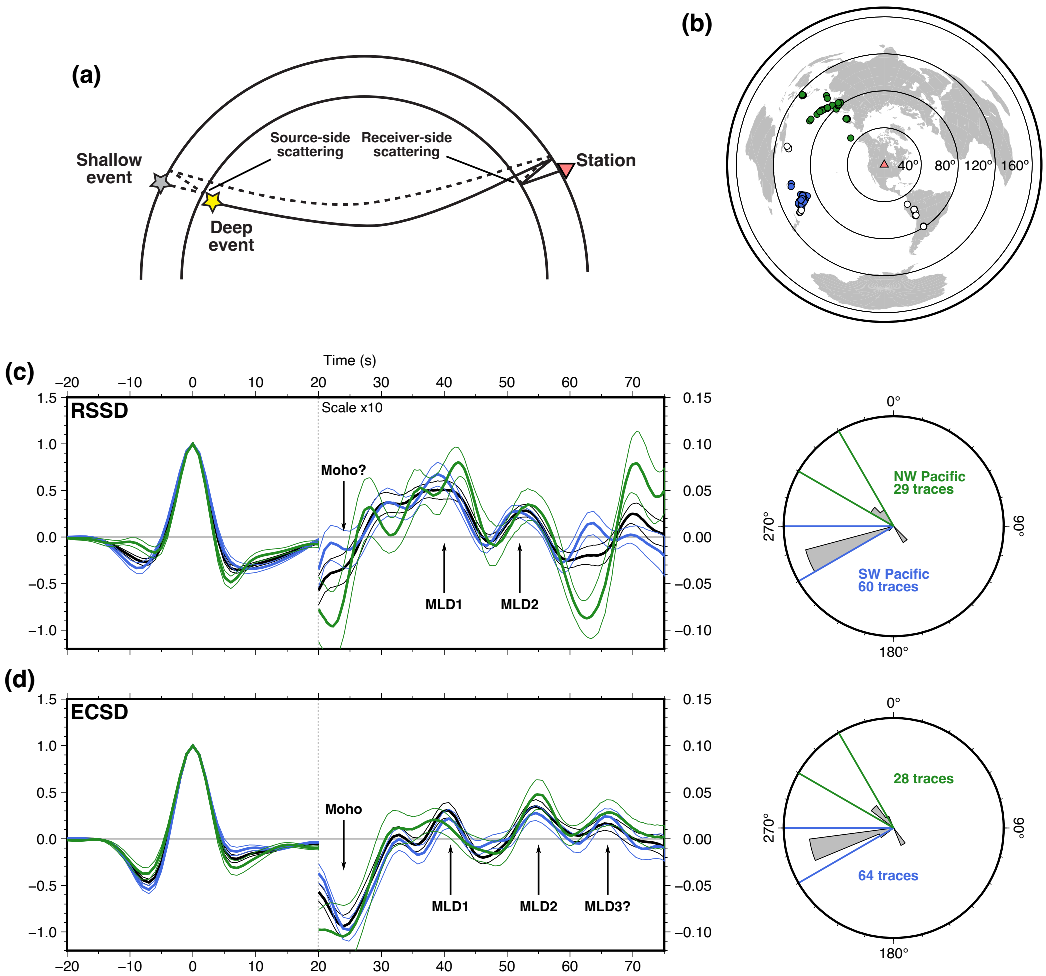

Figure 2. Summary of the method, event distribution, and waveform stacks of the two main back-azimuth windows. (a) Schematic of the difference between using shallow and deep events for SH-reverberation studies. Solid and dashed curves: ray paths of the deep and shallow events, respectively. (b) Distribution of the events used for our analysis. Blue, green, and white circles: events of the southwest-Pacific group, northwest-Pacific group, and others, respectively. (c) and (d): time-domain waveform stacks (left) and event back-azimuth distributions (right) for RSSD and ECSD, respectively. The vertical scale of the window containing the Moho and MLD reverberations is increased by ten times to better show the weak signals. Thick and thin wiggles: the stacks and corresponding uncertainties, respectively. Blue, green, and black wiggles: stacks for the southwest-Pacific group, northwest-Pacific group, and all events, respectively.

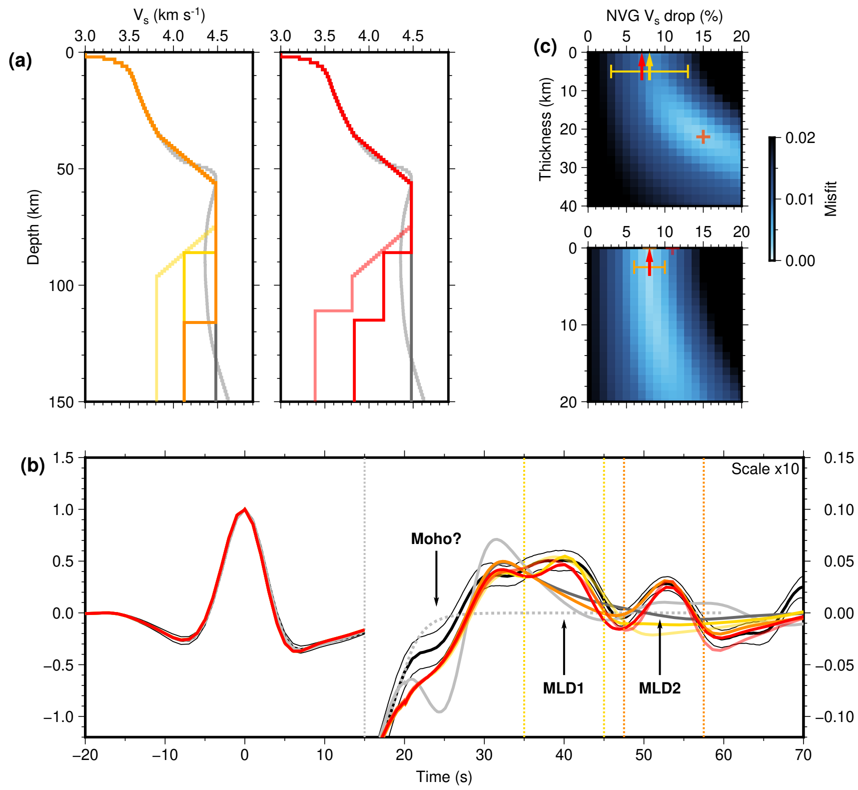

Figure 3. Waveform-fitting for RSSD using 1D isotropic models. (a) V_s models. Light gray: reference models from EFD18. Dark gray: EFD18 models with smoothed Moho velocity gradients and homogenized mantle velocities. Yellow transparent and opaque: best-fit models for the MLD1 window without and with enforcing a zero NVG thickness, respectively. Orange transparent and opaque: best-fit models for the MLD2 window without and with enforcing a zero NVG thickness, respectively. Red transparent and opaque: best-fit models for the combined window without and with enforcing a zero NVG thickness, respectively. (b) Observed and synthetic waveforms. Black thick and thin: observed waveform and uncertainty. Gray dotted: estimated source wavelet. Rest: synthetic waveforms computed using the models colored accordingly in (a). Yellow and orange dotted lines: time windows for computing the misfits for MLD1 and MLD2, respectively. (c) Misfit reductions as functions of percentage V_s drops across the NVG and NVG thicknesses for MLD1 (top) and MLD2 (bottom), respectively. Yellow cross and arrow: best-fit parameter combinations for MLD1 without and with enforcing a zero NVG thickness, respectively. Orange cross and arrow: best-fit parameter combinations for MLD2 without and with enforcing a zero NVG thickness, respectively. Red crosses and arrows: parameter combinations for MLD1 and MLD2 for the combined window without and with enforcing a zero NVG thickness, respectively.

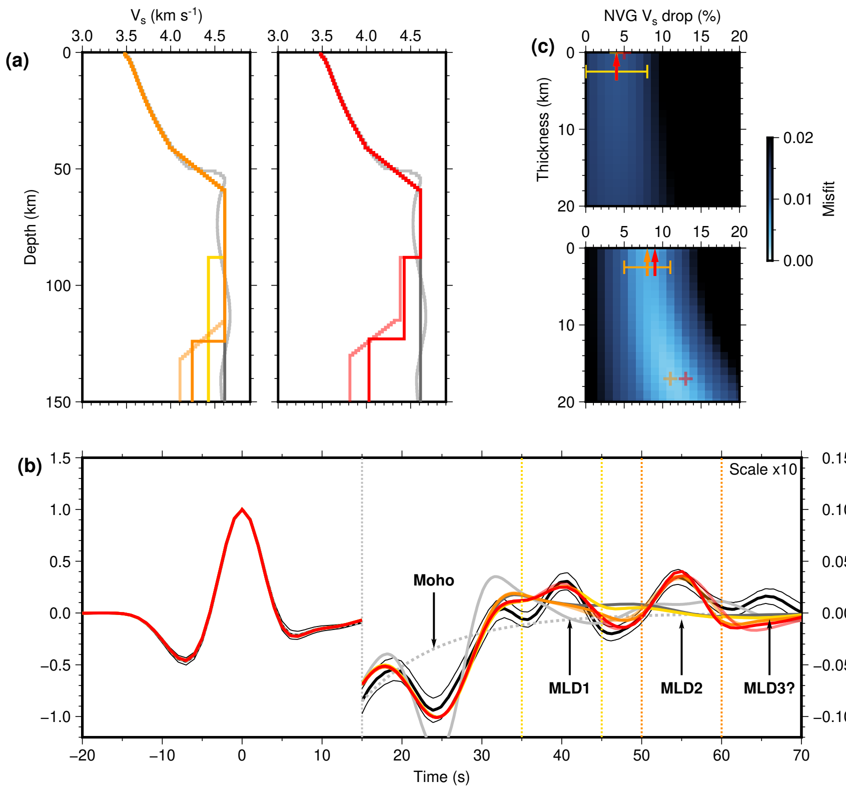

Figure 4. Same as Fig. 3, but for ECSD.

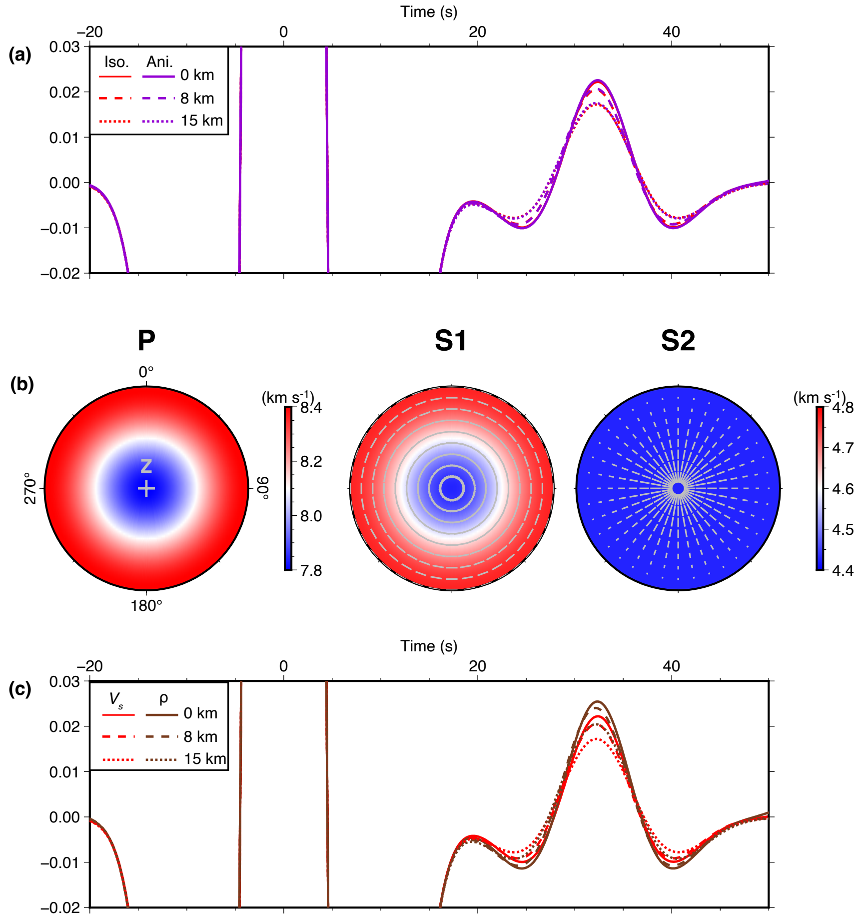

Figure 5. Trade-offs between different factors in determining SH-reflection amplitude. (a) Synthetic SH-reverberation waveforms computed using various layer-over-half space models. Red: models with a 5% isotropic V_s drop in the half space. Purple: models with a 7.5% positive radial anisotropy ($V_{SH} > V_{SV}$) in the half space. Solid, dashed, and dotted: models with gradient-zone thicknesses of 0, 8 and 15 km. (b) Phase-velocity surfaces for the P, fast S (S1), and slow S (S2) waves in the medium with a 7.5% radial anisotropy. Gray bars: projections of S1 and S2 polarization directions onto the horizontal plane. Gray cross: zenith. (c) Same as (a) but for models with isotropic V_s drops and density drops. Red: same as red waveforms in (a). Brown: models with 5% density drop in the half space.

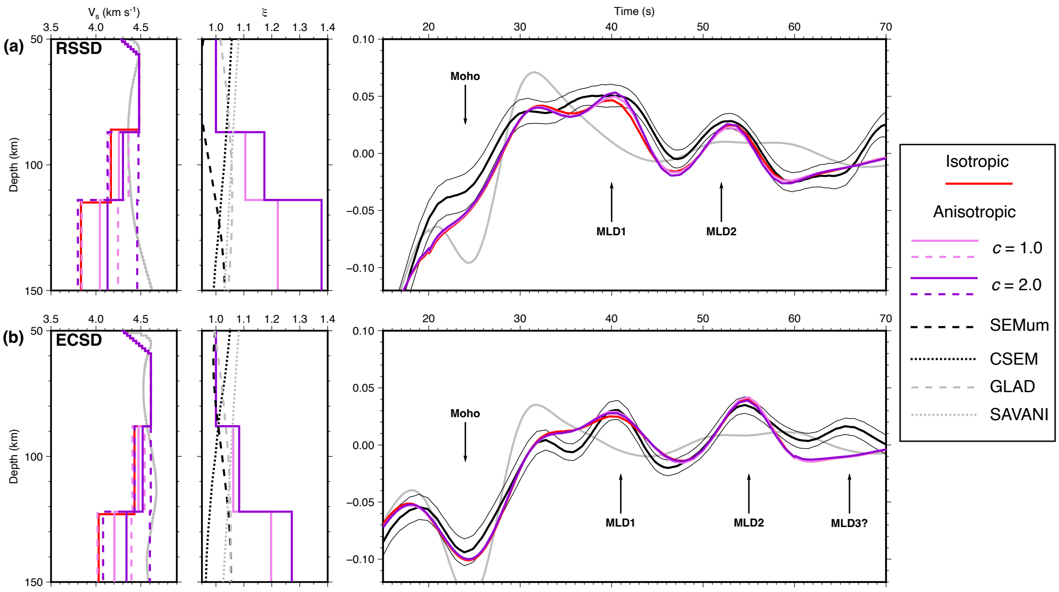

Figure 6. Waveform-fitting using radially anisotropic models for (a) RSSD and (b) ECSD. Left panels: V_s models. Red, light purple, and dark purple solid: best-fit $\bar{V}_s$ for the isotropic model and the anisotropic models with the scaling between $\bar{V}_s$ drop and percentage increase in a $c = 1.0$ and 2.0, respectively. Light purple and dark purple dashed: V_{SH} (high) and V_{SV} (low) for the anisotropic models with $c = 1.0$ and 2.0, respectively. Middle panels: ξ models. Light purple and dark purple: models corresponding to those in the same color in the left panel. Black dashed: *SEMum-NA14* (Yuan et al., 2014). Black dotted: *CSEM_North_America* (Krischer et al., 2018). Gray dashed: *GLAD-M25* (Lei et al., 2020). Gray dotted: *SAVANI_US* (Porritt et al., 2021). Right panels: observed and synthetic waveforms. Red, light purple, and dark purple: synthetic waveforms computed using the models in the same colors. The rest of the objects are the same as those in Figs. 3 and 4.

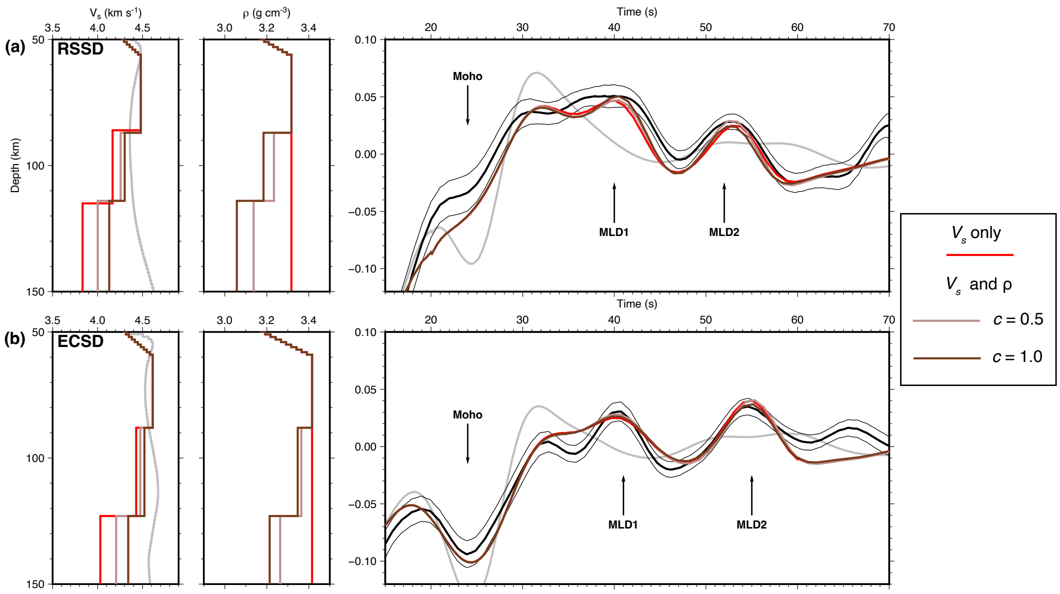

Figure 7. Same as Fig. 6 but showing models with density reductions at the MLDs for (a) RSSD and (b) ECSD. Left panels: V_s models. Red, light brown, and dark brown: best-fit V_s models without density variations and with the scaling between V_s and density drop c = 0.5 and 1.0, respectively. Middle panels: density models. Red, light brown, and dark brown: models corresponding to those in the same color in the left panel. Right panels: observed and synthetic waveforms. Red, light brown, and dark brown: synthetic waveforms computed using the models in the same colors. The rest of the objects are the same as those in Figs. 3 and 4.

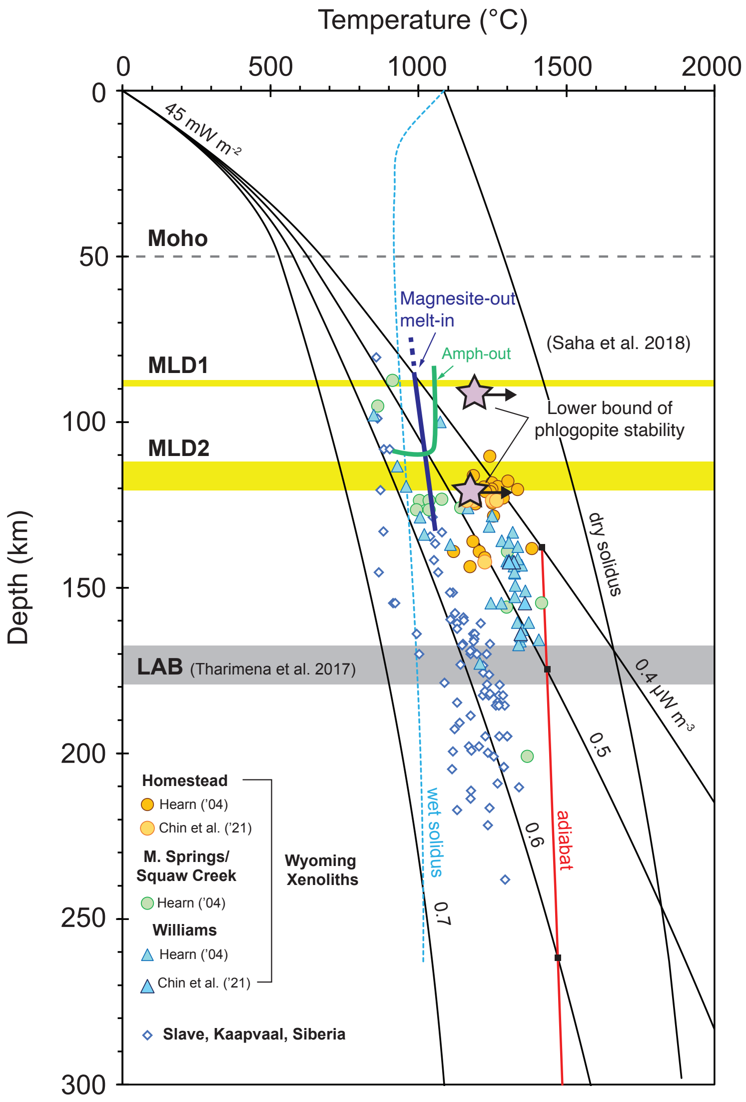

Figure 8. Temperature versus depth plot showing modeled geotherms, xenolith data, phase boundaries, and inferred MLD and LAB depths. Geotherms are computed assuming a surface heat-flow of 45 mW m^{-2}, crustal heat-production rates of 0.4–0.7 µW m^{-3}, a mantle heat-production rate of 0.03 µW m^{-3} (Rudnick et al., 1998), and a crustal thickness of 50 km (this study). The mantle adiabat is from Katsura (2022). Xenolith *P*-*T* data are from the following studies: Slave craton (Kopylova & Caro, 2004; Aulbach et al., 2007), Kaapvaal craton (Gibson et al., 2008; Ionov et al., 2010), Wyoming Craton (Homestead, MacDougal Springs, Squaw Creek, Williams; Hearn Jr, 2004; Chin et al., 2012). Dry and wet (water-saturated) solidi are from Katz et al. (2003).

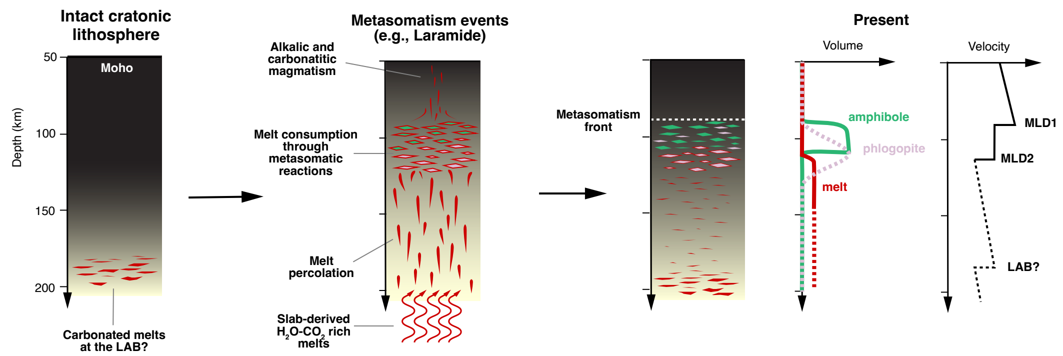

Figure 9. Schematics for the "melt-percolating barrier" model for the origin of MLDs.

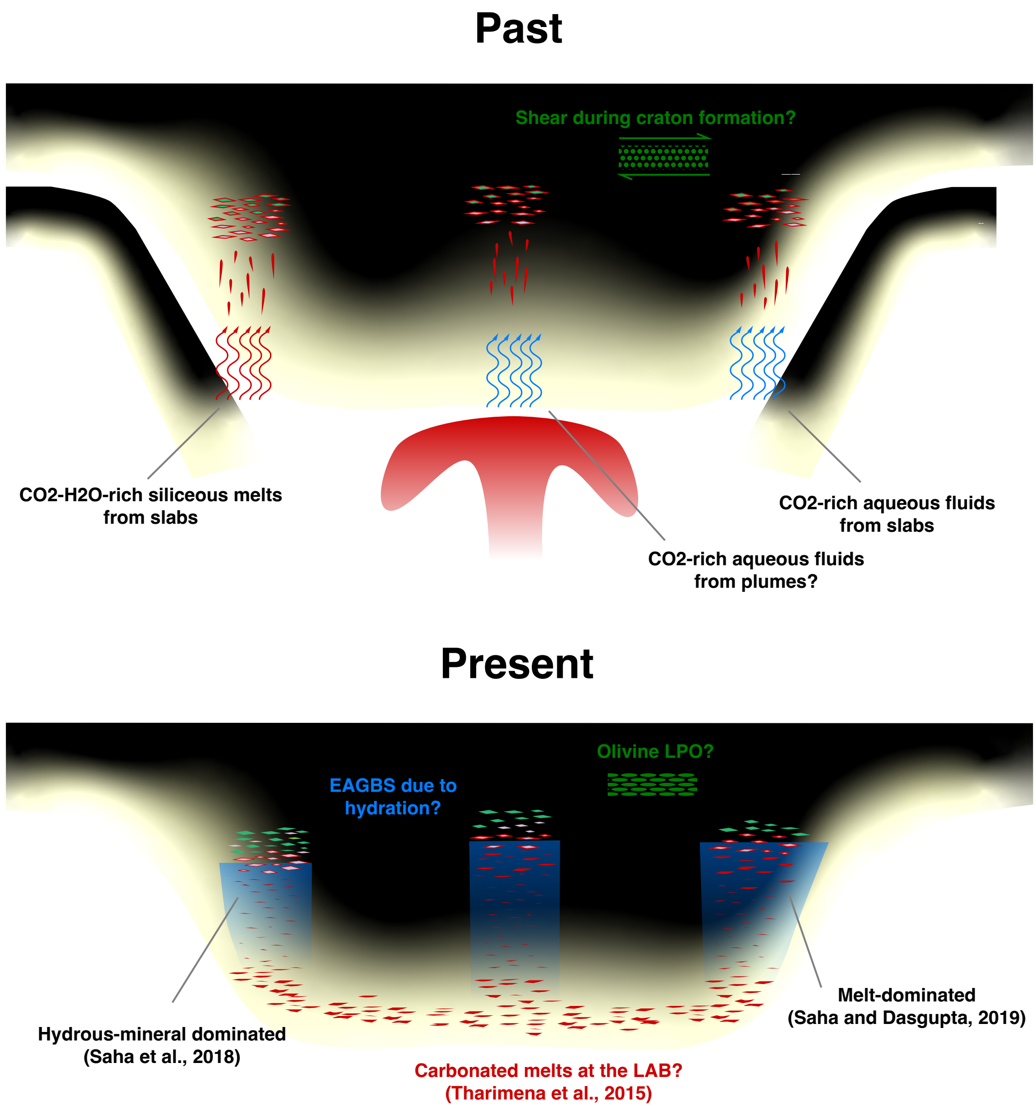

Figure 10. Schematics illustrating the likely diverse origins of the MLDs in different parts of a craton. Note that the different processes in the top panel likely happened during different periods of the craton's life span.